

The Coherent Magnetic Field of the Milky Way

MICHAEL UNGER ^{1,2} AND GLENNYS R. FARRAR ³

¹*Institute for Astroparticle Physics (IAP), Karlsruhe Institute of Technology (KIT), Karlsruhe, Germany*

²*Institutt for fysikk, Norwegian University of Science and Technology (NTNU), Trondheim, Norway*

³*Center for Cosmology and Particle Physics, Department of Physics, New York University, New York, NY 10003, USA*

ABSTRACT

We present a suite of models of the coherent magnetic field of the Galaxy (GMF) based on new divergence-free parametric functions describing the global structure of the field. The model parameters are fit to the latest full-sky Faraday rotation measures of extragalactic sources (RMs) and polarized synchrotron intensity (PI) maps from WMAP and Planck. We employ multiple models for the density of thermal and cosmic-ray electrons in the Galaxy, needed to predict the skymaps of RMs and PI for a given GMF model. The robustness of the inferred properties of the GMF is gauged by studying many combinations of parametric field models and electron density models.

We determine the pitch angle of the local magnetic field ($(11 \pm 1)^\circ$), explore the evidence for a grand-design spiral coherent magnetic field (inconclusive), determine the strength of the toroidal and poloidal magnetic halo fields below and above the disk (magnitudes the same for both hemispheres within $\approx 10\%$), set constraints on the half-height of the cosmic-ray diffusion volume (≥ 2.9 kpc), investigate the compatibility of RM- and PI-derived magnetic field strengths (compatible under certain assumptions) and check if the toroidal halo field could be created by the shear of the poloidal halo field due to the differential rotation of the Galaxy (possibly).

A set of eight models is identified to help quantify the present uncertainties in the coherent GMF – spanning different functional forms, data products and auxiliary input, and maximizing the differences in their predictions. We present the corresponding skymaps of rates for axion-photon conversion in the Galaxy, and deflections of ultra-high energy cosmic rays.

Keywords: Galactic magnetic field, Galactic physics, Milky Way, Cosmic rays

1. INTRODUCTION

Spiral galaxies are known to be permeated by large-scale magnetic fields, with energy densities comparable to the turbulent and thermal energy densities of the interstellar medium; see e.g. Beck (2016) for a recent review. A good knowledge of the global structure of these fields is important for understanding their origin, inferring their effect on galactic dynamics, estimating the properties of diffuse motion of low-energy Galactic cosmic rays, and studying the impact of magnetic deflections on the arrival directions of extragalactic ultrahigh-energy cosmic rays. The GMF is also important for new physics studies, for instance axion-photon conversion in the GMF or the interpretation of possible signatures of astrophysical dark matter annihilation.

The determination of the large-scale structure of the magnetic field of our Galaxy is particularly challenging since one must infer it from the vantage point of Earth, located inside the field. Previous attempts to model the Galactic magnetic field (GMF) are summarized by Jaffe (2019). In this paper, we focus on the coherent magnetic field of the Galaxy, leaving the study of its turbulent component to the near future. Following Jansson & Farrar (2012a) (hereafter JF12), we derive the GMF by fitting suitably general parametric models of its structure to the two astrophysical data sets which are the most constraining of the coherent magnetic fields: the *rotation measures* (RMs) of extragalactic polarized radio sources and the *polarized intensity* (PI) of the synchrotron emission of cosmic-ray electrons in the Galaxy.

The relation of these two astrophysical observables to the magnetic field is detailed in Sec. 2, followed by a description of the RM and PI data in Sec. 3. The interpretation of this data relies on the knowledge of the three-dimensional density of thermal electrons and cosmic-ray electrons in the Galaxy.

We discuss these *auxiliary models* in Sec. 4. The parametric models of the GMF investigated in this paper are introduced in Sec. 5 and the model optimization is described in Sec. 6.

The combination of different data sets, auxiliary models and parametric functions yields an ensemble of GMF models that reflect the uncertainties and degeneracies inherent in the inference of the global field structure from the limited information provided by the RM and PI data. In Sec. 7 we narrow down these model variants to a few benchmark models that encompass the largest differences within the ensemble.

A typical application of the global magnetic field models is the inference of the arrival direction of cosmic rays at the edge of the Galaxy and the determination of the conversion probability of axions in the magnetic field of the Galaxy. In Sec. 8 we briefly comment on the implications of our study on these topics.

We conclude this paper by giving a brief summary of our findings in Sec. 9 and addressing the question: What is known and not known about the coherent magnetic field of the Galaxy?

2. OBSERVABLES

In this work, we derive the global structure of the GMF from two astrophysical observations, Faraday rotation measures and polarized synchrotron intensity. These two quantities provide complementary information on the parallel and perpendicular components of the coherent magnetic field along the line of sight from the observer at Earth through the Galaxy.

The *rotation measure* (RM) relates the Faraday-rotated polarization angle χ of an astrophysical source observed at a wavelength λ to its intrinsic polarization angle χ_0 after passing through the magnetized plasma of the Galaxy via

$$\chi(\lambda) = \chi_0 + \text{RM} \lambda^2. \quad (1)$$

We follow the IAU convention based on [Manchester \(1972\)](#) (see also [Ferrière et al. 2021](#)) in which the RM is positive for a photon traveling in the same direction as the magnetic field points, through an ambient medium with free electrons. In our notation, taking the observer to be at the origin and the positive unit vector \mathbf{u}_r pointing away from the observer, RM is given by

$$\text{RM} = -C_{\text{RM}} \int_0^\infty n_e(\mathbf{x}(r)) \mathbf{B}(\mathbf{x}(r)) \mathbf{u}_r dr,$$

where the position \mathbf{x} at distance r from an observer located at \mathbf{x}_0 is $\mathbf{x}(r) = \mathbf{x}_0 + \mathbf{u}_r r$,¹ n_e denotes the density of the thermal electron plasma in the interstellar medium, and $C_{\text{RM}} = e^3 / (8 \epsilon_0 \pi^2 m_e^2 c^3) \approx 0.8119 \text{ (rad/m}^2\text{)} (\text{cm}^3/\text{pc } \mu\text{G)}$ (e.g. [Bradt 2008](#)). Thus, RM is negative for a magnetic field oriented away from the observer.

The interpretation of RM becomes more complicated if one considers the possibility of a small-scale correlation or anti-correlation of magnetic fields and thermal electrons. An anti-correlation could arise if the magnetic field is in pressure equilibrium with the thermal electron plasma. In this case, the local Faraday rotation would be systematically diminished and interpreting the RM assuming no anti-correlation would underestimate the magnitude of the integrated line-of-sight magnetic field. A positive correlation could be caused by compression enhancing both the magnetic field and electron density. These effects were studied by [Beck et al. \(2003\)](#) (see also ([Seta & Federrath 2021](#))) who provide the following approximate relation between the rotation measure for the uncorrelated case, RM_0 , and the general case with a correlation coefficient κ ,

$$\text{RM} = \text{RM}_0 \left(1 + \frac{2}{3} \kappa \frac{\langle b^2 \rangle}{B^2 + \langle b^2 \rangle} \right), \quad (2)$$

where B denotes the coherent field and $\langle b^2 \rangle$ is the mean squared field strength of the turbulent magnetic field. In one of our model variants we will allow for a non-zero κ .

The *polarized synchrotron intensity* (PI) originates from cosmic-ray electrons and positrons spiraling in the coherent magnetic field of the Galaxy. The observed PI depends on the CR-electron-density-weighted incoherent superposition of synchrotron emission along the line of sight. For long-wavelengths, the effect of Faraday rotation along the path between emission and observation needs to be taken into account. At the magnetic field strengths and frequencies relevant for this analysis (few μG and 30 GHz), the typical cosmic-ray energy responsible for synchrotron emission is of the order of tens of GeV (e.g. [Longair 2011](#)) and the Faraday depolarization is not significant.

The relationship between the synchrotron volume emissivity and the magnetic field strength is particularly simple for the case of electrons with an energy distribution following a

¹Throughout this work, we assume an observer at $\mathbf{x}_0 = \mathbf{x}_\odot = (-r_\odot, 0, z_\odot)$ in a right-handed Galactic coordinate system. The vertical distance of the Sun from the Galactic plane z_\odot is somewhere between 0.006 ± 0.001 kpc ([Joshi et al. 2016](#)) and 0.026 ± 0.003 kpc ([Majaess et al. 2009](#)) and can thus be neglected for the purpose of this work, i.e., we set $z_\odot \rightarrow 0$. For the distance of the Sun to the Galactic center we adopt the precise measurement of the GRAVITY collaboration, $r_\odot = 8.178 \pm 0.025$ kpc ([Abuter et al. 2019](#)).

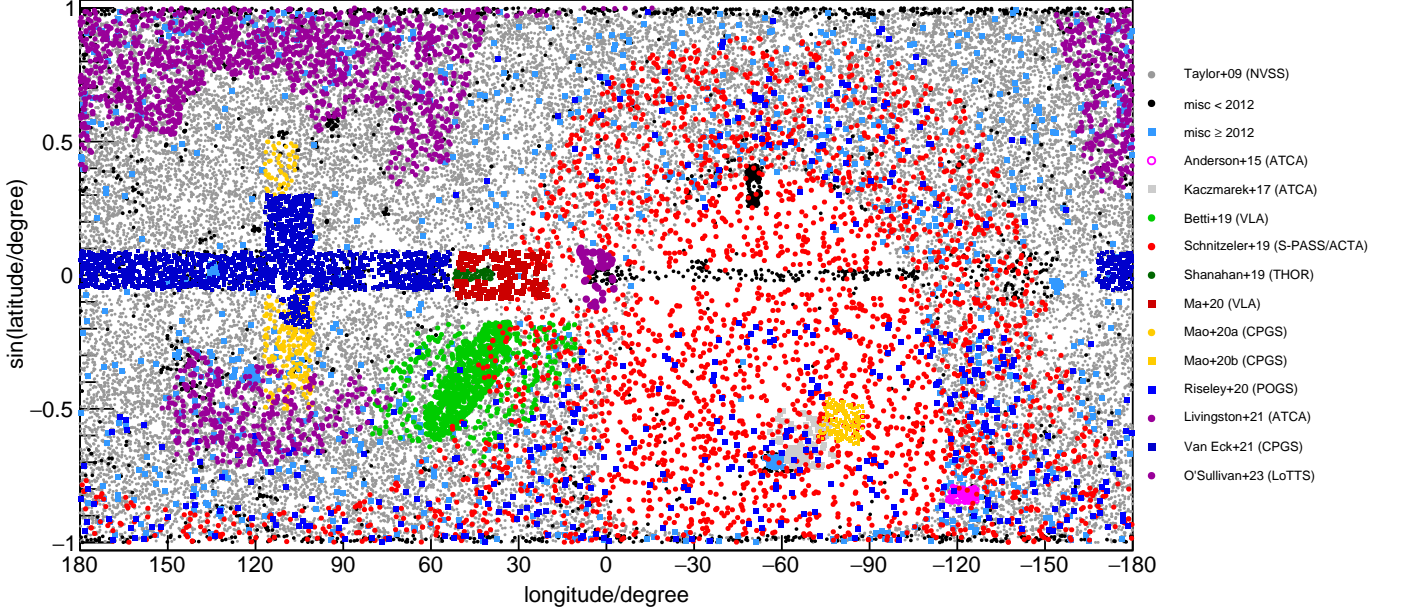


Figure 1. Overview of the RM data used in this analysis. Measurements are shown in Galactic coordinates using a cylindrical projection that visually preserves the point density per solid angle. RMs published before 2012 (and thus available for the JF12 analysis) are shown as gray and black circles.

power-law, $n_{\text{cre}}(E) = n_0 E^{-p}$:

$$j_{\nu} \propto n_0 \nu^{-\frac{-(p-1)}{2}} B_{\perp}^{\frac{p+1}{2}} \stackrel{p=3}{=} n_0 \nu^{-1} B_{\perp}^2, \quad (3)$$

where in the last step the approximation of $p \approx 3$ was used, which is applicable for a canonical E^{-2} spectrum at the source softened to E^{-3} due to energy losses from synchrotron cooling and inverse Compton scattering.

However, the cosmic-ray electron spectrum is not expected to be an exact power law (e.g. Orlando & Strong 2013). To obtain the local volume emissivity at the position \mathbf{x} we therefore integrate the single-electron emissivity over energy,

$$j_{\nu}(\mathbf{x}) = \int_0^{\infty} j(E, B_{\perp}(\mathbf{x})) n_{\text{cre}}(\mathbf{x}, E) dE, \quad (4)$$

where the emissivity $j(E)$ of an electron of energy E is given in Eqs. (8.56) and (8.57) of Longair (2011) and can be conveniently evaluated using the synchrotron functions provided by the [GSL library](#). The integral over the emissivities along the line of sight given the three-dimensional distribution of $n_{\text{cre}}(\mathbf{x}, E)$ and $B_{\perp}(\mathbf{x})$ yields the Stokes parameters Q and U of the polarized synchrotron intensity. Q and U add up quadratically to the total polarized intensity² via

$$\text{PI}^2 = Q^2 + U^2 \quad (5)$$

and their ratio defines the observed polarization angle

$$\psi_{\text{PA}} = \frac{1}{2} \arctan(U/Q). \quad (6)$$

²Note that instrumental noise on Q and U leads to a positive bias in PI when estimated via Eq. (5) (e.g. Wardle & Kronberg 1974). Since we will fit the measured Q and U data, but not PI, the bias is not important for this work.

ψ_{PA} is perpendicular to the line-of-sight average of the n_{cre} -weighted magnetic field angle in the plane of the sky

$$\langle \psi_{\text{mag}} \rangle = \psi_{\text{PA}} + \pi/2, \quad (7)$$

i.e. the analysis of Q and U is sensitive to both the strength and the orientation of the perpendicular projection of the magnetic field along the line of sight.

Isotropic random magnetic fields do not contribute to the polarized intensity, but an anisotropic random field results in a net-polarized intensity, because Q and U define only the plane of polarization, and are thus invariant under a 180° rotation of the magnetic field. Anisotropic random magnetic fields can originate from magneto-hydrodynamic turbulence (Goldreich & Sridhar 1995) or from the stretching or compression of a flux-frozen isotropic random magnetic field (Laing 1980). The latter can lead to basically one-dimensional fluctuations along a preferred orientation, termed “ordered random” by Jaffe et al. (2010) or “striated” by Jansson & Farrar (2012a). A striated random field does not make a net contribution to the RM since the contributions of opposite-sign regions cancel out. However, it does contribute to the polarized synchrotron emission since that depends only on the orientation and not the direction of the field. Jansson & Farrar (2012a) considered different values of the striation factor for different components of the field, but found to be all the same. Here we model the possible striation via a simple spatially independent multiplicative factor to the coherent field,

$$B' = (1 + \xi)B. \quad (8)$$

The striation factor ξ is related to the striation factor β used in JF12, for which a cosmic-ray electron energy spectrum with a spectral index of $p = 3$ was assumed, via $(1 + \xi) = \sqrt{1 + \beta}$.

3. DATA PRODUCTS

3.1. Rotation Measures

We assemble a sky map of extragalactic RMs based on individual measurements from various catalogues and surveys as illustrated in Fig. 1. Most of the currently known extragalactic RMs were derived by Taylor et al. (2009) from the two-band polarization data of the NVSS survey (Condon et al. 1998) leading to 37 543 RMs with a declination of $> -40^\circ$. Since only two frequencies are available in this data set, the derived RMs are susceptible to $n\pi$ ambiguities in Eq. (1) for high values of $|\text{RM}|$. We replace the values of 20 of these high-RM sources by the ones obtained by the broadband follow-up observations of Ma et al. (2019), three are discarded based on these re-observations.

For measurements predating the year 2014, we use the catalogue of 4553 high-quality RMs curated by Xu & Han (2014). Notable surveys with $N_{\text{RM}} > 100$ collected in this catalogue are from Simard-Normandin et al. (1981), Broten et al. (1988), Brown et al. (2003), Klein et al. (2003), Broderick et al. (2007), Brown et al. (2007a), Heald et al. (2009), Feain et al. (2009), Mao et al. (2010), Van Eck et al. (2011), Mao et al. (2012a), and Mao et al. (2012b).

3220 RMs in the Southern equatorial hemisphere are taken from the S-PASS/ATCA wide-band radio polarimetry survey (version 0.9) of Schnitzeler et al. (2019) (applying the quality cuts given in Sec. 4 of that paper and requiring emission at a single Faraday depth as well as model fits with $\chi^2/\text{ndf} < 10$). This survey is of particular significance, since it complements the sky coverage of the NVSS survey. GMF model fits predating the S-PASS/ATCA release, e.g. JF12, were constrained by only a very small amount of RMs in the 18% southernmost equatorial sky.

Further 5999 RMs published in the years 2014–2022 are taken from the data compilation of Van Eck et al. (2023) (v1.1.0 at Van Eck et al. 2022). Notable surveys with $N_{\text{RM}} > 100$ in this compilation are from Farnes et al. (2014), Anderson et al. (2015), O’Sullivan et al. (2017), Kaczmarek et al. (2017), Betti et al. (2019), Riseley et al. (2020), Ma et al. (2020), and Van Eck et al. (2021). In addition, we include the recent 2461 extragalactic RMs of O’Sullivan et al. (2023).

In this data set of 53 773 RMs, we identify obvious multiple measurements of the same extragalactic object if their coordinates correspond to the same pixel id on a high-resolution

HEALPIX sky map with $N_{\text{side}} = 2048$.³ All duplicate RMs but the measurement with the best frequency coverage are dropped, leaving 47 054 RMs of unique extragalactic objects.

In the next step of data selection, we apply a two-pass algorithm to reject outliers caused by either a large source-intrinsic RM or a wrong resolution of the $n\pi$ -ambiguity. The procedure is similar in spirit but different in detail to that used for the data set of JF12. For each RM measurement we accumulate surrounding measurements within an angular collection radius starting at 1° . The collection radius is increased until a sample of at least 10 independent surrounding RM measurements are found that differ by less than three median absolute deviations from the median RM of that sample. In the second pass, these sources are then used to calculate the mean and standard deviation of the RM in the region surrounding each object. We keep objects if their RM value is closer than three standard deviations from the surrounding mean.

The remaining 44 857 RMs are displayed in Fig. 2a. For this figure, we show the average of RMs in an $N_{\text{side}} = 32$ HEALPIX map,⁴ in-painting 1524 pixels (12%) without a measurement. At this somewhat higher resolution than the one used for the analysis (see below), both the large and small-scale features of the extragalactic rotation measures are visible. The most salient large-scale features of the RM sky are known since the early advent of RM catalogues, see e.g. the discussion in (Andreasyan & Makarov 1988; Han et al. 1997): For the inner Galaxy (longitudes between -90 to 90°) there is an anti-symmetry in both longitude and latitude of the sign of the average rotation measures, whereas in the outer Galaxy (longitudes from 90° to 270°), the average RMs have the same sign above and below the plane, as summarized by the following schematic of an RM sky map,

$$\text{RM}(\ell, b) \approx \begin{pmatrix} - & + & - & + \\ - & - & + & + \end{pmatrix}. \quad (9)$$

In addition, many small-scale features can be identified, some of which can be attributed to foreground objects. We remove some of the most obvious regions, indicated by circles in Fig. 2b. Firstly, we discard lines of sight if they pass

³The HEALPIX package (Hierarchical, Equal Area, and iso-Latitude Pixelation of the sphere) is used to subdivide the sky into equal-area pixels (Górski et al. 2005). The resolution N_{side} of a HEALPIX map is related to the number of pixels via $N_{\text{pix}} = 12N_{\text{side}}^2$. For a map with $N_{\text{side}} = 16$, the standard resolution used in this paper, the number of pixels is $N_{\text{pix}} = 3072$ with an angular width of approximately $\theta \approx \sqrt{4\pi/N_{\text{pix}}} 180^\circ/\pi = \sqrt{3/\pi} 60^\circ/N_{\text{side}} = 3.66^\circ$.

⁴This and subsequent maps shown in this paper are area-preserving Mollweide projections of the sky in Galactic coordinates with the Galactic center at the origin. The longitude increases towards the left from 0° at the center towards $+180^\circ$ and decreases towards the right from $+360^\circ$ at the center to $+180^\circ$ (or, equivalently, from 0° to -180°).

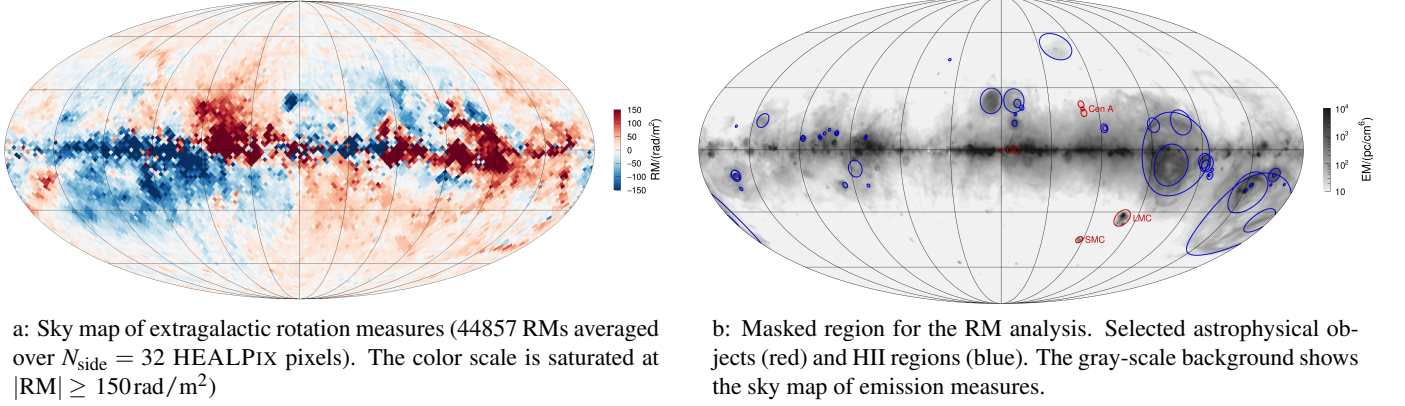


Figure 2. Sky map of rotation measures (left) and masked regions (right).

through magnetized objects with a large angular size, i.e. M31, the Small and Large Magellanic Cloud, Centaurus A (core and lobes) and the Galactic Center. The excluded regions around these objects are shown in red in Fig. 2b. Secondly, we deselect RMs if the thermal electron density along the line of sight is dominated by a single object. Such local overdensities in the diffuse WIM are caused by the ultraviolet light of young massive stars ionizing the interstellar medium around them, creating an HII region. RMs in lines of sight passing through HII regions are often dominated by the product $n_e B_{\parallel} \Delta$ inside the region of thickness Δ , see e.g. Heiles et al. (1981) and Harvey-Smith et al. (2011). These RMs are thus not representative of the large-scale GMF. Regions of locally enhanced thermal electron density can e.g. be identified by the emission measure, $\text{EM} = \int_0^{\infty} n_e dl$, which is displayed in Fig. 2b based on the composite of H α surveys (VTSS, SHASSA and WHAM) from Finkbeiner (2003). More than 8000 Galactic HII regions are known in the Galaxy (Anderson et al. 2014), but most of them are either far away, and thus of small angular extent, and/or at low Galactic latitudes, where the overall RM integral through the plane is large enough that it is not overshadowed by the contribution of a single HII region. We therefore deselect only the lines of sight that overlap with an HII region if it is either of large angular extent ($r > 10^\circ$) or at high latitudes, $|b| > 5^\circ$. These regions are displayed in blue in Fig. 2b if their size is $> 0.5^\circ$.

The final 41 686 RMs are then binned in 3072 angular pixels of an $N_{\text{side}} = 16$ HEALPIX map with an angular diameter of $\sim 3.7^\circ$. For each pixel, we calculate the mean and unbiased sample variance to be used in the model optimization (see Eq. (48) below). If the number of RMs within one pixel is < 10 , then the variance (but not the mean) is calculated using the 10 RMs with the closest angular distance to the center direction of the pixel. This leads to 2838 pixels with RM data, where 46 pixels are excluded because no data was observed in this direction and another 188 pixels are excluded by the masks displayed in Fig. 2b. The final masked and binned RM data are shown in Fig. 10 in Sec. 7.

3.2. Polarized Synchrotron Emission

The polarized synchrotron emission from the Galaxy is best observed at high frequencies, where the depolarization of the signal due to Faraday rotation is negligible. At Faraday depths typical for the Galaxy, the change in polarization angle becomes negligible in the tens of GHz range, see Eq. (1). The received polarized intensity in units of Rayleigh-Jeans antenna temperature, $T = c^2 / (2\nu^2 k_B) \text{PI}$, decreases as ν^{β_s} with frequency. Here the synchrotron spectral index $\beta_s \approx -3$ for a cosmic-ray electron spectrum with index $p = 3$, see Eq. (3). Another source of polarized emission from the Galaxy originates from thermal dust with a spectral index of $\beta_d \approx +1.6$ (Ade et al. 2015). Empirically, the cross-over between the two components is at around 100 GHz.

The “sweet spot” for the observation of synchrotron emission is therefore at high enough frequencies such that Faraday depolarization is negligible, but not too high, such that the signal is not dominated by polarized dust emission. The WMAP and PLANCK satellites operated in this frequency regime, with a frequency threshold of 20 and 30 GHz respectively.

From WMAP we use the final nine-year results (DR5) on the polarized synchrotron emission at 22.5 GHz provided at a HEALPIX resolution of $N_{\text{side}} = 64$ (Bennett et al. 2013). Four variants of Q and U sky maps are available, differing mainly by the constraints placed on β_s during analysis. These four variants of the derived polarized synchrotron intensity are in good agreement outside of the Galactic plane, which is anyway masked in our analysis (see below). We use the “base” model, which is the most data-driven variant in which the synchrotron spectral index was allowed to float freely in each sky pixel. We in-paint the pixels that are flagged as having an erroneous component separation (2.7%) with the Q and U averages of their eight surrounding neighbor pixels.

From PLANCK we use the third release (R3.0) of the polarized synchrotron foreground at 30 GHz derived from component separation using the COMMANDER software (Akrami

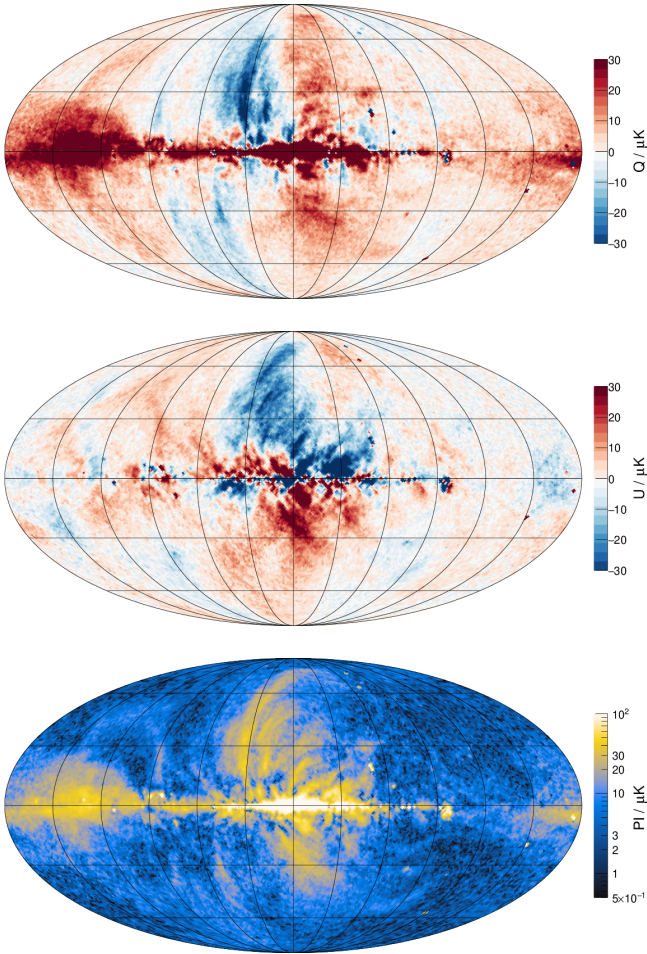


Figure 3. Stokes Q (top panel) and U (middle panel) parameters and polarized intensity PI (bottom panel) from the averaged synchrotron maps of PLANCK and WMAP at 30 GHz.

et al. 2020). These sky maps are provided at high resolution of $N_{\text{side}} = 2048$ and we average the Q and U values to obtain maps with $N_{\text{side}} = 64$ to match the resolution of WMAP. During this averaging, spurious outliers in the high-resolution maps are identified and discarded if the value is more than 5σ away from the median of the values within the low-resolution pixel. This procedure removes 0.18% of the high-resolution data points.

We then combine the Q and U sky maps from WMAP and PLANCK into a lower resolution map at $N_{\text{side}} = 16$ by taking the simple arithmetic average of all 32 measurements in each pixel (16 from each experiment). WMAP intensities are extrapolated to the PLANCK frequency with a spatially-constant synchrotron spectral index of $\beta_s = -3.15$ based on the mean value predicted by our simulations described in Sec. 4.2. Note that due to the proximity of the WMAP and PLANCK frequencies, even a large difference between the actual and assumed of $\Delta\beta_s = 0.2$ would introduce a variation in extrapolated intensity of only $1 - (22.5 \text{ GHz} / 30 \text{ GHz})^{\pm\Delta\beta_s} = \pm 6\%$.

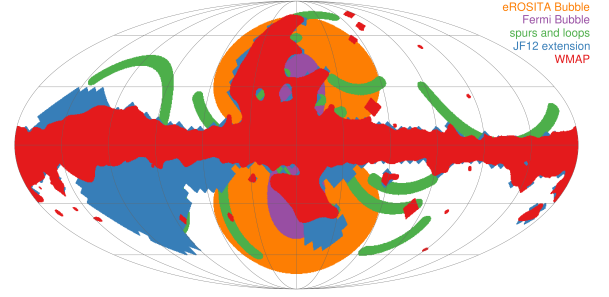


Figure 4. Polarized synchrotron mask used in this analysis. Masked regions are shown in red, blue and green (see text). For comparison, the outline of the Fermi and eROSITA bubbles are shown in violet and orange.

The variance of the 32 data points per pixel is used to calculate the weights in the χ^2 minimization as discussed in Sec. 6.

The Stokes parameters derived by the WMAP and PLANCK collaborations exhibit systematic large-scale differences, see Fig. 22 in the appendix. These differences could either be attributed to large-scale spatial variation of the synchrotron spectral index or to residual calibration uncertainties in one or both of the data sets. A combined analysis of WMAP and PLANCK data was recently presented by the COSMOGLOBE Collaboration (Watts et al. 2023a,b), performing the component separation and the calibration of the data sets simultaneously. We will use the COSMOGLOBE results as an alternative to our average and study the effect on the parameters of GMF models in Sec. 7.

Our combined maps of Stokes Q and U and polarized intensity PI of the Galactic synchrotron emission at 30 GHz are shown in Fig. 3. As can be seen, both Q and U exhibit large-scale features, which we will in the following interpret as imprints of the large-scale features of GMF. However, care must be taken not to include regions with strong local features that could bias our fits. We therefore mask-out some regions of the sky in fitting to the GMF parameters.

The elements of our mask when fitting the polarized intensity data are shown in Fig. 4. Red indicates the map used in the original WMAP analysis. It excludes regions of high polarized intensity along the Galactic plane and the North Polar Spur, and pixels containing strong extragalactic sources such as the radio lobes of Centaurus A. The blue region depicts the additional polarized intensity mask introduced by Jansson & Farrar (2012a) mainly to remove a presumably local, high-latitude polarized emission at $90^\circ < \ell < 180^\circ$. Finally, we also mask the green regions as an attempt to remove further large circular arcs (called loops, spurs, or filaments) visible in PI. Here we exclude data in the direction of loops I to IV, as defined by Berkhuijsen et al. (1971) and further filaments identified by Vidal et al. (2015). The union of the above leads to our final PI mask. The cumulative application of these

three masks leaves 73.1% (WMAP), 63.4% (WMAP + JF12), and 57.8% (WMAP + JF12 + loops) of the sky for analysis.

It is worthwhile noting that the exact attribution of features in the polarized radio sky to local or global phenomena in the Galaxy is still under debate, see e.g. [Lallement \(2022\)](#). Some of the loops and filaments could be caused by local supernova remnants expanding into the surrounding ambient magnetic field ([Spoelstra 1973](#)), whereas others might be related to large-scale magnetized outflow from the Galactic center ([Carretti et al. 2013](#)), related to the so-called “Fermi bubbles” observed in gamma rays ([Ackermann et al. 2014](#)) and surrounded by “eROSITA bubbles” in X-rays ([Predehl et al. 2020](#)). These are shown as violet and orange regions in Fig. 4, demonstrating that our mask retains some directions which contain contributions from the Fermi and eROSITA bubbles.

4. AUXILIARY MODELS

4.1. Thermal Electrons

The magnetized plasma responsible for the Faraday rotation of extragalactic radio sources resides mostly in the warm ionized medium (WIM) of the Galaxy (e.g. [Ryden & Pogge 2021](#)). To interpret the rotation measures, a three-dimensional model of the density, $n_e(\mathbf{x})$, of these free thermal electrons is needed. Here we use two models of n_e : NE2001 of [Cordes & Lazio \(2002\)](#) and YMW16 of [Yao et al. \(2017\)](#). Both models were tuned to describe the *dispersion measure* DM of Galactic pulsars, which is given by the line-of-sight integral from Earth to the pulsar at a distance d , $DM = \int_0^d n_e(\mathbf{x}(r)) dr$. More than 3000 pulsars with measured DMs are listed in the current version (1.70) of the ATNF pulsar catalogue ([Manchester et al. 2005](#)), but only for a few the distance d is well known: NE2001 was tuned to the DMs of 112 pulsars and YMW16 used 189. Given the large number of parameters of these models (e.g. the YMW16 model has 82 fixed parameters and 32 fitted parameters) and the scarcity of data, they rely, to a large extent, on astrophysical priors for the geometrical topology of the thermal electron density.

Particularly important for the modeling of the large-scale structure of the GMF is the vertical structure of the Galactic WIM which is relatively well constrained by the DMs of pulsars in high-latitude globular clusters [Gaensler et al. \(2008\)](#). Since the fit of NE2001 pre-dates most of this data, we replace the original value of the exponential scale height of the diffuse WIM of $h_{WIM} = 0.95$ kpc with $h_{WIM} = 1.3 \pm 0.2$ kpc as derived by [Schnitzeler \(2012\)](#) for this model. A larger value of $h_{WIM} = 1.67 \pm 0.05$ kpc was inferred by [Yao et al. \(2017\)](#) for their YMW16 model.

An illustration of the thermal electron densities of YMW16 and NE2001 is shown in Fig. 5. As can be seen, the two models differ substantially, especially regarding the positions

and widths of spiral arms, the density in the molecular ring at $r \approx 5$ kpc and in the Galactic Center, and concerning the scale-height of the thick disk of the WIM. Whereas YMW16 can predict pulsar DMs with a somewhat higher fidelity than NE2001, the latter model remains a viable alternative to describe the large-scale features of the WIM (e.g. [Price et al. 2021](#)). By using both models in our GMF fits, we can study the systematic effects arising from different assumptions on the thermal electron density.

4.2. Cosmic Ray Electrons

Calculating Galactic synchrotron emission requires not only a model of the GMF but also a model of the three-dimensional density distribution and energy spectrum of cosmic-ray electrons in the Galaxy, $n_{cre}(\mathbf{x}, E)$.

In contrast to the purely phenomenological thermal electron models discussed in the previous section, predictions of n_{cre} are based on detailed modeling of the production and propagation of electrons and positrons in the Galaxy (e.g. [Moskalenko & Strong 1998](#)), to obtain a steady-state solution of the diffusion equation of cosmic rays in the Galaxy ([Ginzburg & Syrovatskii 1964](#)). In its simplest version (sometimes referred to as “plain diffusion”), the defining quantity of the model is the diffusion coefficient of charged particles in the interstellar medium (ISM). Most calculations assume a homogeneous and isotropic Galactic diffusion coefficient D within a “diffusion volume” approximated as a cylinder of half-height h_D .

The normalization and rigidity⁵ dependence of D is determined from measurements of the fluxes of secondary and primary cosmic-ray nuclei at Earth. The most precise estimates (in terms of the uncertainty of both cosmic-ray flux and nuclear cross sections) are derived from the ratio of the flux of secondary boron nuclei and (mostly) primary carbon nuclei. However, secondary-to-primary ratios can only constrain the ratio, D/h_D , (e.g. [Maurin et al. 2001](#)). Estimates of D/h_D in a plain diffusion scenario range from 0.03 kpc/Myr ([Génolini et al. 2019](#); [Yuan et al. 2017](#)) to 0.10 kpc/Myr ([Cummings et al. 2016](#)) at a reference rigidity of 10 GV.

The degeneracy between h_D and D can in principle be broken by data on “cosmic clocks” (e.g. $^{10}\text{Be}/^9\text{Be}$ or Be/C), but due to the poor quality of current data and uncertainties in the spallation cross sections, only mild constraints on the halo height can be derived and the current estimates of h_D are in the range 2 to 10 kpc (e.g. [Weinrich et al. 2020](#); [Evoli et al. 2020](#); [Maurin et al. 2022](#)). We therefore consider diffusion volumes having $h_D = 2, 4, 6, 8$ and 10 kpc and derive the corresponding n_{cre} for each, to allow us to assess the uncertainty in the GMF due to the present uncertainty in h_D . For

⁵The rigidity of a particle with charge Ze and momentum p (energy E) is $\mathcal{R} = pc/(Ze) \simeq E/(Ze)$

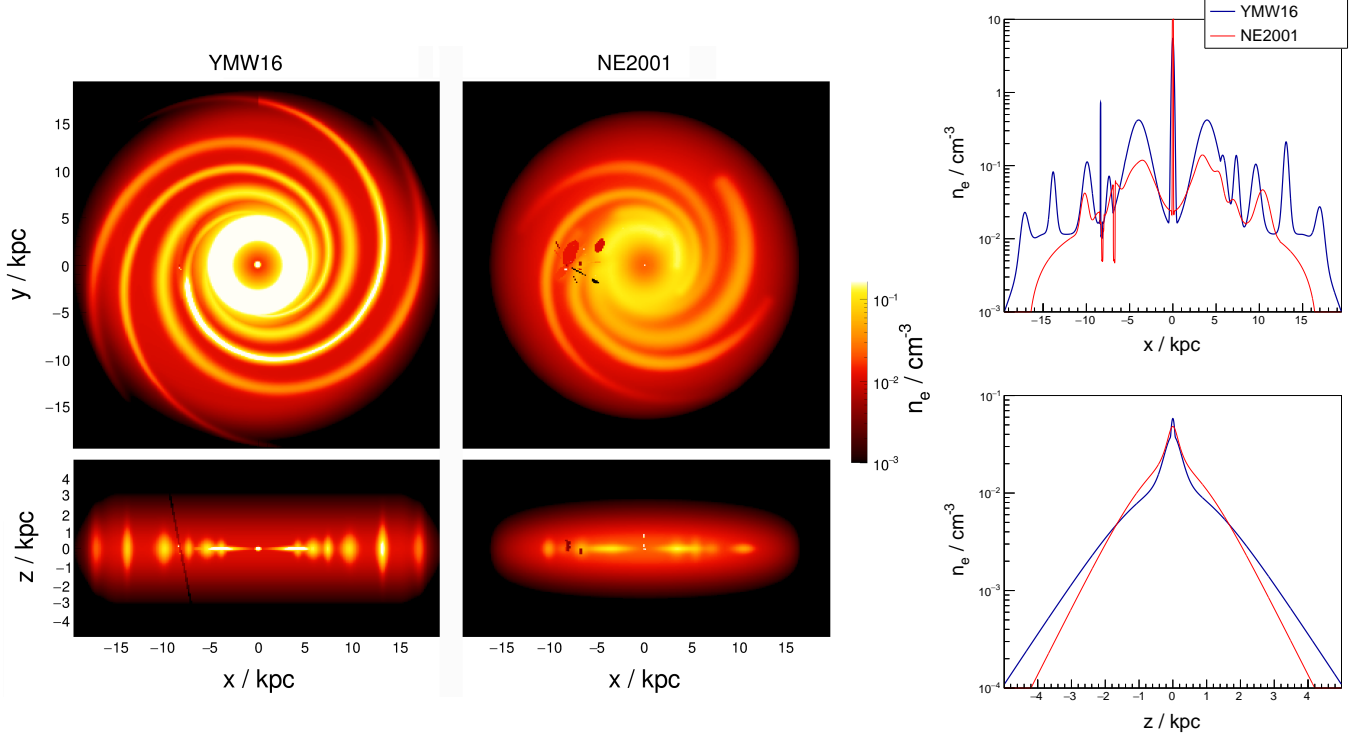


Figure 5. *Left:* Thermal electron density, n_e , for the YMW16 and NE2001 model. The top panel shows the mid-plane density at $z = 0$ and the bottom panel gives an edge-on view of the density at $y = 0$ in the $x-z$ plane. Structures visible at around the position of the sun ($\approx (-8.2, 0, 0)$ kpc) are due to the modeled under- and over-densities of the local interstellar medium. *Right:* Thermal electron density along the Galactic x -axis at $z = y = 0$ (top) and along the z -axis at $x = -6$ kpc and $y = 0$.

each of the five different values of the height of the diffusion volume, h_D , we solve the cosmic-ray diffusion equation with the DRAGON program (Evoli et al. 2008).⁶

For each value of h_D we obtain the diffusion coefficient at 10 GV from $D/h_D = 0.046$ kpc/Myr and we take the rigidity dependence of $D(\mathcal{R})$ to be the one derived for the “PD2” model of Cummings et al. (2016). At high rigidities ($\mathcal{R} \gtrsim 5$ GV) the diffusion coefficient scales as $D \propto \mathcal{R}^{-0.578 \pm 0.073}$, i.e. compatible with the power-law scaling $\mathcal{R}^{-1/2}$, typical for a turbulent magneto-hydrodynamical cascade (Iroshnikov 1964; Kraichnan 1965). The spatial distribution of Galactic cosmic-ray sources is taken to follow the radial distribution of pulsars in the Galaxy (Lorimer et al. 2006), used as a proxy for the distribution of supernova remnants, and we use the JF12 magnetic field model to calculate the cooling of cosmic-ray electrons due to synchrotron radiation. The maximum galactocentric radius of the diffusion volume was set to $R_{\text{max}} = 18$ kpc.

We constrain the solutions of the diffusion equations by the measurements of cosmic-ray proton and lepton fluxes, in the

local interstellar medium from the Voyager I satellite (Cummings et al. 2016), and inside the heliosphere from AMS-02 orbiting Earth on the International Space Station (Aguilar et al. 2014, 2015, 2019). We first find the proton spectrum at the source; this then fixes the contribution to the lepton flux at Earth coming from proton interactions with cosmic rays and the ISM ($p_{\text{CR}} + p_{\text{ISM}}$), accounting for a small adjustment due to contributions from nuclei. We then attribute the remaining lepton flux to the injected lepton spectrum. Thus, in this simplified ansatz, the well-known “positron anomaly” (Adriani et al. 2009), i.e., the excess of positron flux beyond expectations from secondary production at energies $\gtrsim 10$ GeV, is attributed to the injected lepton spectrum. Such an ansatz is plausible if astrophysical sources of primary positrons have a similar spatial distribution as the sources of primary electrons, e.g., if pulsars are the sources of the “anomalous” positrons and electrons (Hooper et al. 2009) and the bulk of electrons is accelerated in supernova remnants. Then, if the interest is only in the sum of electrons and positrons, as it is in our case, the two sources can be lumped together into a single source class. Due to the fast cooling time of electrons and positrons at high energies, the high-energy flux at Earth might be dominated by a local source and thus not representative of the average lepton flux in the Galaxy (e.g. Di Mauro et al. 2014; Joshi & Razaque 2017; Mertsch 2018). How-

⁶We choose DRAGON over the other widely used solver GALPROP (Strong & Moskalenko 1998) because at the time of setting up our analysis chain only DRAGON supported spatially varying diffusion coefficients. In this paper we, however, investigate only homogenous diffusion.

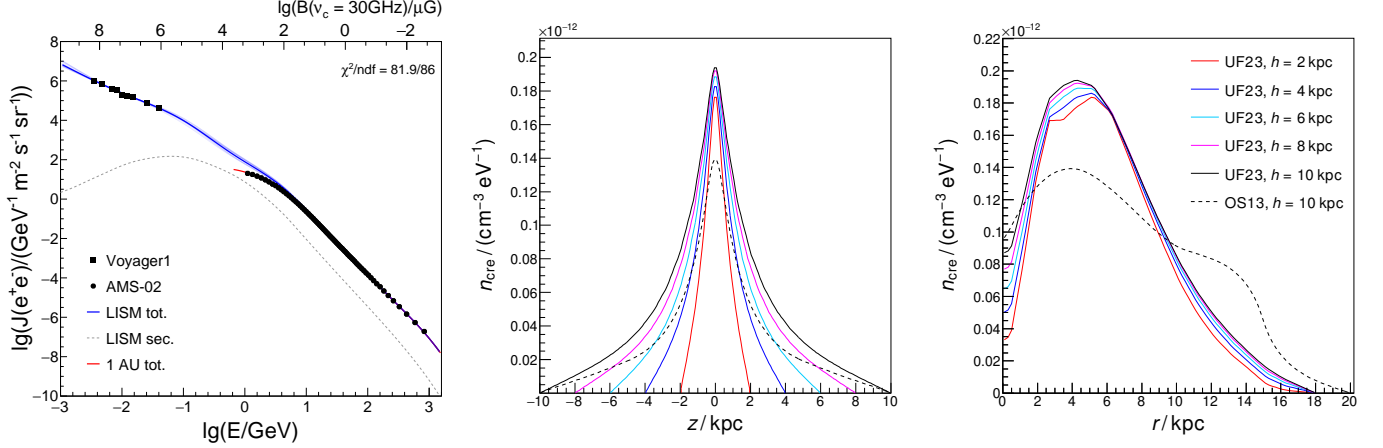


Figure 6. *Left:* Flux of cosmic-ray electrons and positrons at Earth. Black points show the measurements. The calculated flux in the local interstellar medium (LISM), for the $h_D = 6$ kpc case, is shown as a blue band and the contribution from secondary production ($p_{CR} + p_{ISM}$ interactions) is indicated by a dashed line; the solar-modulated flux at Earth is shown as a red line. The additional x -axis at the top of the figure shows the magnetic field strength needed to obtain a synchrotron peak at $\nu_c = 30$ GHz (i.e., the frequency for which the Planck collaboration reports the polarized synchrotron emission), for the electron energy given in the x -axis at the bottom of the figure. *Middle:* Density of 10 GV cosmic-ray electrons at a galactocentric radius $r = 4$ kpc, as a function of Galactic height z and *Right:* as a function of radius r at mid-plane ($z = 0$). Different choices of the half-height h_D of the diffusion volume are shown as lines with different colors. The dashed line is the result of Orlando & Strong (2013) for $h_D = 10$ kpc.

ever these effects are expected to play a role only above 100 GeV and are thus not important for the synchrotron frequencies of interest in this study. An example of our fit of the cosmic-ray lepton flux is shown in the left panel of Fig. 6.

As a further systematic check, we also interpret the synchrotron data using the z10LMPDE cosmic-ray electron model, a GALPROP calculation of Orlando & Strong (2013) (OS13) used in (Adam et al. 2016) for GMF modeling (Jaffe 2017). This model assumes a half-cylinder height of $h_D = 10$ kpc, a maximum radius of $R_{\max} = 20$ kpc and the source distribution from Strong & Moskalenko (1998) with a radial cutoff at 15 kpc. Further differences to our fiducial GALPROP calculation include a different magnetic field (Sun & Reich 2010) for electron cooling and a different value of $D/h_D = 0.031$ at 10 GV. We normalized this model to match the AMS flux of electrons and positrons at 35 GV.

The vertical and radial distribution of the cosmic-ray lepton density at 10 GV for different values of h_D and the OS13 model are shown in the middle and right panel of Fig. 6. As expected, a larger half-height of the diffusion volume leads to a larger cosmic-ray occupation in the halo, while the density in the disk is approximately constant due to the normalization at Earth. The different source distribution assumed for OS13 results is mainly responsible for the very different radial distribution of cosmic ray leptons.

Of course, further variations beyond the scale height are possible and we studied the effect on synchrotron maps of several other type of variations, as described below. However only the variation of h_D makes a significant change in

the PI predictions outside of the mask we use, so we only include the six n_{cre} models outlined above in our GMF model fitting.⁷ A spiral distribution of sources can affect the PI up to 25% in the Galactic plane, but has negligible effects outside of the polarization mask used in this work. Using the PLANCK-tune of the JF12 random field (Adam et al. 2016) for synchrotron cooling instead of the original model (Jansson & Farrar 2012b) affects the intensity by up to 16% in the outer Galaxy (where a spiral arm with a large random field is present in the original model to describe the intensity from the “fan region”), but the differences are again negligible outside the masked region used in this paper. The same holds for n_{cre} models using a three-dimensional model of the interstellar radiation field from Porter et al. (2017). Moreover, in this study we did not iteratively re-adjust the magnetic field used for the synchrotron energy losses in the n_{cre} calculations. But the resulting refitted coherent fields are of the same order of magnitude as the ones of JF12 and therefore the electron cooling is dominated by the sum of contributions from the random magnetic field and inverse Compton scattering. Finally, it was shown by Orlando (2018) that the cosmic-ray electron spectrum above a few GeV is insensitive to the inclusion of re-acceleration and/or convection in the diffusion equation, therefore we do not consider it here.

⁷Note that in the framework of a tunable striation parameter, an overall factor in the polarized synchrotron intensity does not affect the derived coherent magnetic field, but only the striation factor.

The six models shown in Fig. 6 will be used in this paper to study the systematic effect of the three-dimensional model of n_{cre} on the derived structure of the GMF.

We note that future systematic studies should include an investigation of the effects of a more realistic particle propagation with an inhomogeneous and/or anisotropic diffusion coefficient (e.g. Di Bernardo et al. 2013; Giacinti et al. 2018; Merten et al. 2017; AL-Zetoun & Achterberg 2018), ideally with a self-consistent description of relation between the magnetic field and the diffusion coefficient (e.g. Kühlen et al. 2022; Blasi 2023).

5. MAGNETIC FIELD MODELS

5.1. General Considerations

The goal of this work is provide the best possible analytic approximation to the large scale coherent GMF, given the limitations of present data and other required input. To this end, we describe the field as a superposition of functions that are general enough to capture the main large scale features of its structure.

Inspired by previous models of the coherent Galactic magnetic field (e.g. Stanev 1997; Prouza & Šmída 2003; Sun et al. 2008; Pshirkov et al. 2011; Jansson & Farrar 2012a) we describe the global structure of the GMF as a superposition of a large-scale halo field and a logarithmic spiral field in the Galactic disk beyond a minimum radius. The halo field is composed of a toroidal and a poloidal field as introduced by Jansson & Farrar (2012a). The need for each of these components to describe large-scale features of the RM and PI sky is discussed in Sec. 7. In this section, we give a brief overview of the different parametric descriptions investigated in this paper and note ways in which the actual coherent GMF is simpler than the most general case.

5.2. Disk Field

5.2.1. General features

The observations discussed above of synchrotron polarization patterns in face-on external spiral galaxies, as well as the RMs of Galactic pulsars, suggest that the coherent field of the Milky Way follows a spiral pattern close to the disk, outside a few kpc from the Galactic center. A logarithmic spiral is inherently divergence-free making it an attractive functional form.

In several previous GMF models the magnetic field was assumed to be organized in “arms” with a pre-defined geometry with the pitch angle α fixed to a value motivated by that of the spiral matter density of the Milky Way (see e.g. Brown et al. 2007b; Jaffe et al. 2010; Jansson & Farrar 2012a; Han et al. 2018). The magnitude and sign within each arm was adjusted to match the data, with the total radial flux being constrained to be zero. Within a given arm, the field was

approximated to be azimuthally constant, leading to strong discontinuities at the boundaries of the arms.

For a fixed-thickness disk with logarithmic-spiral arms, flux conservation implies the field $\sim r^{-1}$, leading to an unphysical singularity at the origin. Therefore the field in such models was assumed to vanish or transition to a purely toroidal configuration at some inner radius.

It should be noted that although the total radial flux vanishes for both the outer logarithmic spiral and inner toroidal regions, the radial flux does not vanish locally in the spiral arm region whereas it does vanish locally in the inner region. Therefore, the flux lines must microscopically be reorganized in some transition region at the boundary. This structure is physically plausible due the mechanical action of the Galactic bar, which extends several kpc from the Galactic center and rotates significantly faster than the disk. The turbulence in the plasma due to the stirring of the bar entangles field lines which at larger radius are ordered. In the inner, stirred region these field lines either contribute to B_{rand} or reconnect, converting magnetic energy to thermal energy.

Global radial flux conservation is compatible with a non-zero toroidal coherent field in the inner zone, but in the picture above the toroidal field strength would be small apart from fluctuations amplified by dynamo action. We allowed for a possible toroidal disk field in the inner Galaxy and found it to be consistent with zero (consistent with previous fits by Jansson & Farrar (2012a)) so we dropped it from the modeling. In the next subsections we describe our two basic models for the disk field, and variants we also investigated.

5.2.2. Fourier Spiral

Here we introduce a new description of the spiral arms of the disk field, that provides flexibility to fit the geometry of the magnetic arms and also avoids discontinuities between them. To specify the spiral disk field, we need fix the pitch angle α , the width and angle of each arm at some reference radius, and the strength of each arm. For this purpose, we decompose the magnetic field strength at reference radius $r_0 = 5$ kpc, as a function of angle ϕ_0 , into n modes of strength B_m and phase ϕ_m :

$$B(r_0, \phi_0) = \sum_{m=1}^n B_m \cos(m(\phi_0 - \phi_m)). \quad (10)$$

The magnetic field in cylindrical coordinates at position (r, ϕ, z) is given by

$$B_d = (\sin \alpha, \cos \alpha, 0) \frac{r_0}{r} B(r_0, \phi_0) h_d(z) g_d(r), \quad (11)$$

where the ϕ_0 corresponding to the given (r, ϕ) is found by following the field line along the logarithmic spiral from (r, ϕ) to the reference radius r_0 , the relation being

$$\phi_0 = \phi - \ln(r/r_0) / \tan \alpha. \quad (12)$$

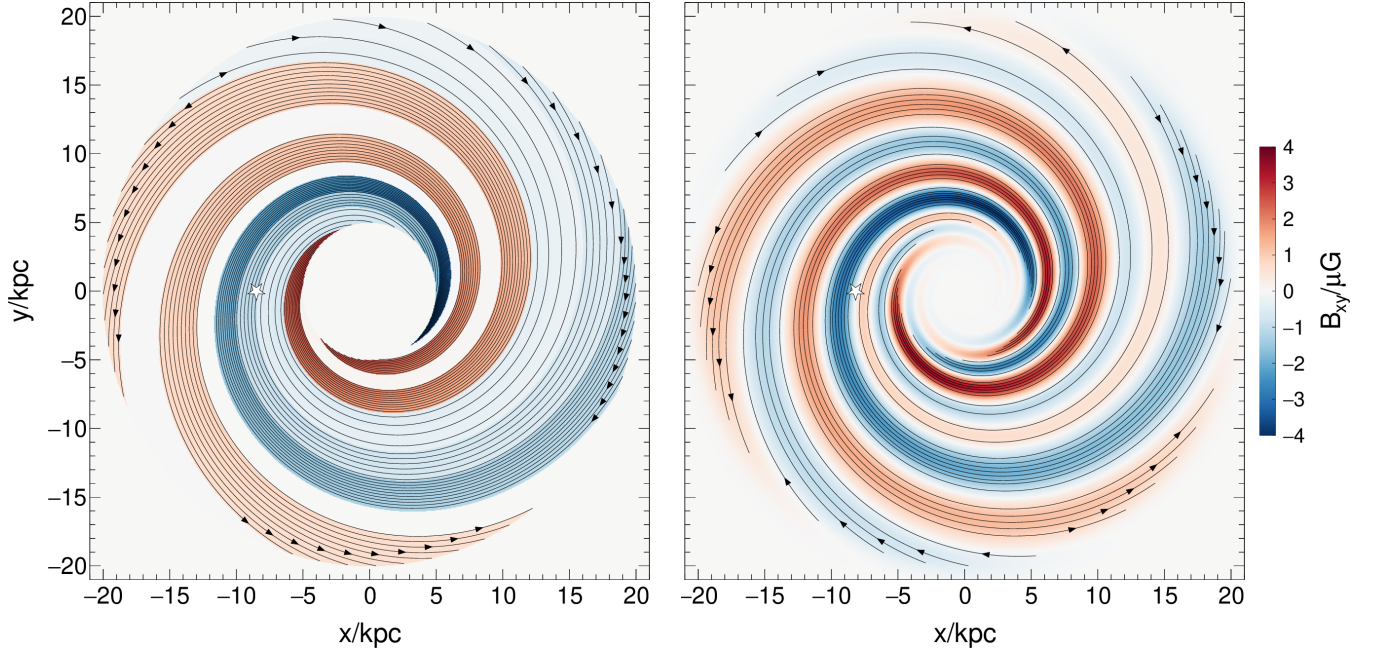


Figure 7. *Left:* Fixed-arm spiral disk field of the JF12 model. *Right:* Fourier spiral of the “neCL” model, see Sec. 7. The position of the sun is indicated with a star.

Due to the expansion of $B(r_0, \phi_0)$ being in terms of a cosine series, we refer to this model of the disk field as “Fourier spiral” in the following. The solenoidality of this field model for $g_d(r) = 1$ is assured because for each mode in Eq. (10) the same amount of flux enters and exits along the circle at r_0 and, due to the $\frac{r_0}{r}$ factor in Eq. (11), the magnetic flux in each arm is constant as a function of radius.⁸ Independently of $g_d(r)$, the total radial flux in this disk field model vanishes for every radius.

The functions $h_d(z)$ and $g_d(r)$ describe the fade-in and fade-out of the field in the vertical and radial direction, respectively. We choose the ansatz

$$h_d(z) = 1 - \sigma\left(\frac{|z| - z_d}{w_d}\right) \quad (13)$$

and

$$g_d(r) = \left[1 - \sigma\left(\frac{r - r_2}{w_2}\right)\right] \sigma\left(\frac{r - r_1}{w_1}\right) (1 - e^{-r^2}), \quad (14)$$

where $\sigma(x)$ denotes the logistic sigmoid function,

$$\sigma(x) = \frac{1}{1 + e^{-x}}, \quad (15)$$

such that the disk field is suppressed to half of its value at z_d , r_1 and r_2 , and the suppression rate is given by the corresponding transition widths. The additional factor $(1 - e^{-r^2})$

⁸Inclusion of an axisymmetric component of the $m = 0$ component implies a net inward or outward flux of the disk field. This excess flux would necessarily flow into the halo and imply a net vertical flux, but we do not find evidence of that in the data, see Sec. 7.6.

is needed to assure that the factor $g_d(r)/r$ in Eq. (11) goes to 0 at $r = 0$.

Note that mathematically $g_d(r)$ violates the solenoidality of the field and is thus to be understood as an effective modeling of the behavior of the disk field at small and large radii. At large radii we expect that the coherent magnetic flux gradually spreads out as the plasma confining it to the disk merges into the circumgalactic medium. At some point the field is so weak and the electron densities so low that our observables are not sensitive to it. We represent this by an effective outer distance r_2 . In the inner Galaxy, within a radius designated r_1 , we expect that the coherent log spiral structure is replaced by a region of low coherent field or possibly a weak toroidal field, as discussed in the previous subsection.⁹

For consistency with the outer radius of the molecular ring in the YMW16 model, in this analysis we set r_1 to 5 kpc; we fixed r_2 to 20 kpc having checked that the fit is insensitive to the exact choice. For the transition widths, we adopt $w_1 = w_2 = 0.5$ kpc. Whether the details of the inner transition can be constrained by the data is left for future work. Without loss of generality, we set the reference radius to $r_0 = 5$ kpc, such that the coefficients B_m in Eq. (10) denote the amplitude of the modes in the inner Galaxy.

⁹Further possibilities include that the magnetic flux of the disk field exits vertically in the inner Galaxy (Ferrière & Terral 2014) (but see ⁸) or that the inward- and outward-going field lines of the disk field connect at r_1 and r_2 as investigated by Kleimann et al. (2019). Both of these configurations entail regions of very high coherent field which would be energetically disfavored, so we did not pursue them.

An example of a Fourier spiral disk field is shown in the right panel of Fig. 7 and for comparison a fixed-arm spiral field is displayed in the left panel. Apart from obvious differences in the arm topologies and field strengths, which are mostly due to different data sets used to fit these models, it can be seen that the Fourier spiral results in a smooth disk field without the discontinuities inherent in the previous fixed-arm models.

5.2.3. Spiral Spur

As an alternative model to the grand-design magnetic spiral implied by the Fourier spiral, we investigate if a localized spiral segment can describe the data equally well. Such an isolated magnetic “spiral spur” in the disk is seen e.g. in Fig. 2 of the cosmological simulation of Pakmor et al. (2014), due predominantly to a local compression of field lines.

We model a spur as a Gaussian of width w_S at reference radius r_0

$$B(r_0, \phi_0) = B_1 \exp\left(-\frac{1}{2}((\phi_0 - \phi_1)/w_S)^2\right), \quad (16)$$

where ϕ_1 denotes the center of the spur and the angle ϕ_0 follows again from the logarithmic spiral via Eq. (12). The field of the spur in cylindrical coordinates is, similar to Eq. (11), given by

$$B_S = (\sin \alpha, \cos \alpha, 0) \frac{r_0}{r} B(r_0, \phi_0) h_d(z) g_S(\phi), \quad (17)$$

where instead of using the radial attenuation $g_d(r)$, the size of the spur is determined from its angular center ϕ_C and angular half-length L_C . We attenuate the magnetic field at $\phi = \phi_C \pm L_C$ with

$$g_S(\phi) = 1 - \sigma \left(\frac{\Delta(\phi, \phi_C) - L_C}{w_c} \right). \quad (18)$$

In the following, we use a fixed attenuation width of $w_c = 5^\circ$ and, without loss of generality, $r_0 = 8.2$ kpc, such that the parameter $B_{0,S}$ is close to the magnetic field strength at the center of the spur, if it is located in the proximity of the solar radius, which is the main focus of the spiral spur model. The superficial lack of flux conservation is understood as a transition between locally compressed and a more complex, broadly-distributed flux distribution not captured in the global model function.

5.2.4. Further Considerations Regarding the Disk Field

Further variations to the Fourier spiral and spiral spur models were studied, but not included in the fiducial models presented in this paper. We investigated a circular “ring field” at small galacto-centric radii. Such a field was introduced in JF12 at $3 \text{ kpc} < r < 5 \text{ kpc}$ with an estimated field strength of $0.1 \pm 0.1 \mu\text{G}$. Here we confirmed that a ring field does not significantly improve our fits and therefore we did not include it in our fiducial models.

We also investigated the sensitivity of the data to the particular choice of $h_d(z)$ and found no significant changes when replacing the logistic sigmoid with a Gaussian ($\Delta\chi^2 = -3$) and a slightly worse description when using an exponential ($\Delta\chi^2 = +30$).

Furthermore, we studied a flaring disk field, i.e. an increase of the vertical extent of the disk with galacto-centric radius as e.g. observed for the atomic hydrogen of the disk (Kalberla & Kerp 2009). We also added the Galactic warp as determined by Levine et al. (2006) to the disk field model. Neither of the two variations improved our preliminary fits reported in (Unger & Farrar 2019) and we therefore do not include them in this analysis.

A model variant we did not explore here is to allow a net inward or outward flux in the disk which is balanced by flux entering the disk due to an imbalance in the N-S halo fields; this was checked by Khurana (2016) for the JF12 model and the flux transfer was found to be consistent with zero, compatible with our findings on the symmetry of the halo field as reported in Sec. 7.6 below.

5.3. Halo Field

Our knowledge of the global structure of the magnetic halo of Milky Way-like galaxies relies on a combination of edge-on observations of external galaxies and high-latitude rotation measures and radio emission (for a review see, e.g., Haverkorn & Heesen 2012).

The large-scale antisymmetric features of extragalactic rotation measures, cf. Eq. (9) and Fig. 2a, follow naturally from a large-scale toroidal¹⁰ field of opposite sign above and below the plane, leading to the observed pattern in RM when superimposed with the local spiral arm of the disk field, schematically

$$\begin{array}{c} \text{---} + \text{---} + \\ \text{---} - + + \end{array} = \begin{array}{c} + + \text{---} - \\ - - + + \end{array} + \begin{array}{c} - \quad + \\ - \quad + \end{array}. \quad (19)$$

$\text{RM}_{\text{tot}} \qquad \text{toroidal halo} \qquad \text{local arm}$

In addition, the large-scale patterns of the Q and U parameters, in particular the tilted nature of the corresponding polarization vectors, can be explained by the presence of an addition poloidal halo component, as suggested by Jansson & Farrar (2012a) who introduced a coherent “X-field” halo component inspired by the X-shaped radio polarization halos observed in edge-on spiral galaxies (e.g. Krause et al. 2020).

Here we will model the magnetic halo of the Galaxy either by a superposition of a separate toroidal and poloidal field, or by a unified halo model, as described below.

¹⁰Here we use the term toroidal field synonymously with a purely azimuthal field, $\mathbf{B} = (0, B_\phi, 0)$, while the term poloidal field denotes a vector field with a vertical but not an azimuthal ϕ -component, $\mathbf{B} = (B_r, 0, B_z)$.

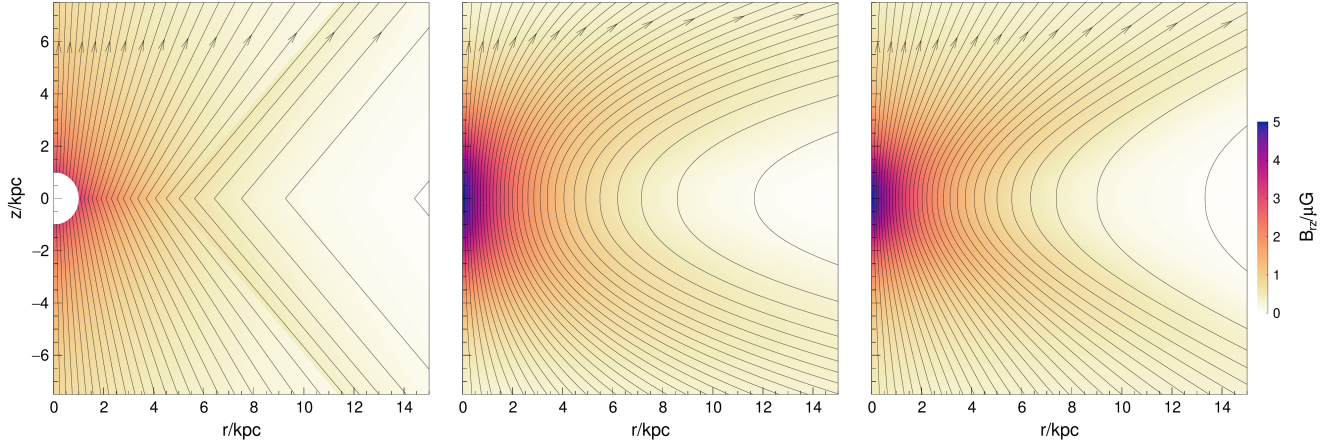


Figure 8. X-field models: JF12 (left), power-function (middle) and coasting X-field (right).

5.3.1. Toroidal Halo

For the toroidal field, we adopt the logistic-exponential ansatz (“ $\sigma_r \exp_z$ ”) of JF12. It is a purely azimuthal field,

$$\mathbf{B}_t = (0, B_\phi, 0) \quad (20)$$

in cylindrical coordinates, with

$$B_\phi = (1 - h_d(z)) e^{-\frac{|z|}{z_t}} \times \left(1 - \sigma \left(\frac{r - r_t}{w_t} \right) \right) \begin{cases} B_N & z > 0 \\ B_S & \text{otherwise} \end{cases} \quad (21)$$

where z_t is the exponential scale height of the toroidal field and the radial cutoff of the toroidal halo is modeled by a logistic sigmoid function with a transition at r_t and a width w_t . The maximum field strength above and below the Galactic plane are given by B_N and B_S , respectively; h_d is defined in Eq. (13), i.e., the toroidal halo field is phased in by the complement of the function that phases out the disk field.

Whereas in JF12 the radial extent of the Northern and Southern halo was allowed to be different, we use only one value r_t , since our preliminary fits showed only a minor deterioration of the fit quality when enforcing a symmetric toroidal (Unger & Farrar 2018). We also checked whether the data is fit better with independent functions $h_d(z)$ for the disk and the halo separately, but found similar transition heights for the disk and halo, even if they were allowed to take on different values.

5.3.2. Poloidal Halo

Jansson & Farrar (2012a) introduced a coherent “X-field” model that is purely vertical at $r = 0$ and becomes increasingly tilted with increasing radius until reaching a constant asymptotic angle with respect to the Galactic plane, $\theta_X \sim 50^\circ$, at a radius of $r_X \sim 5$ kpc. With this model a good description of the polarized synchrotron data could be achieved.

However, this X-field parametrization has three types of discontinuities: one in the inner Galaxy, one at the Galactic plane at $z = 0$ and one at $r = r_X$, as can be seen in the left panel of Fig. 8. These discontinuities are avoided by the improved X-field models described in the following.

A) Power-function X-field— Ferrière & Terral (2014) employed a useful method to construct poloidal field models using Euler potentials. Given the equation of field lines in the form of $r = f(a, z)$ starting midplane at a radius a (i.e. $f^{-1}(r = a) = 0$), the divergence-free cylindrical components of the poloidal field ($B_\phi = 0$) are given by

$$B_r = -\frac{a}{r} B_0(a) \frac{\partial a}{\partial z} \quad (22)$$

and

$$B_z = \frac{a}{r} B_0(a) \frac{\partial a}{\partial r} \quad (23)$$

where any function $B_0(a)$ of the radial dependence of the z -component of the field at $z = 0$ will preserve the solenoidality of the field.

We extend their parabolic “model C” for the z -evolution of the field lines to arbitrary powers p ,

$$r = a(1 + |z/z_p|^p), \quad (24)$$

corresponding to a midplane radius of

$$a(r, z) = \frac{r}{1 + |z/z_p|^p}. \quad (25)$$

Using Eqs. (22) and (23), the radial and vertical field components are

$$B_r = p \frac{z a^3}{r^2 z_p^p} |z/z_p|^{p-2} B_0(a) \quad (26)$$

and

$$B_z = \frac{a^2}{r^2} B_0(a) \quad (27)$$

for $p \geq 1$. In Sec. 7 we will study several possibilities for the radial midplane dependence of the field strength,

$$B_0(a) = B_p f_X(a), \quad (28)$$

with normalization constant B_p and one of the following radial functions:

- exp: $f_X(a) = e^{-\frac{a}{r_p}}, \quad (29)$

- gauss: $f_X(a) = e^{-\frac{1}{2}(\frac{a}{r_p})^2}, \quad (30)$

- sech2: $f_X(a) = \text{sech}^2(a/r_p), \quad (31)$

- logistic: $f_X(a) = 1 - \sigma((a - r_p)/w_p), \quad (32)$

where sech denotes the hyperbolic secant, $\text{sech}(x) = 1/\cosh(x) = 2/(e^x + e^{-x})$ and σ is the logistic sigmoid function defined in Eq. (15).

An example of a power-function X-field is shown in the middle panel of Fig. 8 (for $p = 2.2$ and an exponential radial dependence with $r_p = 2.8$ kpc). As can be seen, the discontinuities present in the original JF12 X-field are avoided, but it differs qualitatively from the JF12 X-field in that the field lines become more and more parallel to the Galactic plane as the radius increases rather than reaching an asymptotic angle.

B) Coasting X-field—A “coasting X-field” with parallel field lines beyond a certain reference radius a_c can be achieved by choosing the field-line equation

$$r = \left(a^n + c \frac{a^n}{a^n + a_c^n} |z|^p \right)^{\frac{1}{n}}. \quad (33)$$

The positive solution for a^n is¹¹

$$a^n = \frac{1}{2} \left(\sqrt{\Delta^2 + 4a_c^n r^n} - \Delta \right), \quad (34)$$

where $\Delta = a_c^n + c|z|^p - r^n$. Inserting it into Eqs. (22) and (23), the radial and vertical field components are obtained as

$$B_r = B_0(a) \frac{c a^2 p z |z|^{p-2}}{n r \sqrt{\Delta^2 + 4a_c^n r^n}} \quad (35)$$

and

$$B_z = B_0(a) \left(\frac{r}{a} \right)^{n-2} \frac{a^n + a_c^n}{\sqrt{\Delta^2 + 4a_c^n r^n}}. \quad (36)$$

In this paper we study X-fields for the special case $p = n$ for which Eq. (33) becomes

$$r = a \left[1 + \frac{1}{1 + (a/a_c)^p} \left(\frac{|z|}{z_p} \right)^p \right]^{\frac{1}{p}}, \quad (37)$$

¹¹Note that $\sqrt{x^2 + k} - x$ is of low numerical accuracy if $k \ll x$. Instead we use $(\sqrt{x^2 + k} - x) \frac{\sqrt{x^2 + k} + x}{\sqrt{x^2 + k} + x} = \frac{k}{\sqrt{x^2 + k} + x}$ in our numerical implementation.

and Eqs. (35) and (36) simplify accordingly. The new parameter z_p is given by $z_p = \frac{a_c}{c^{1/p}}$. For large values of the coasting radius a_c ($a \ll a_c$) this three-parameter function simplifies further to the two-parameter equation

$$r = a \left[1 + \left(\frac{|z|}{z_p} \right)^p \right]^{\frac{1}{p}}. \quad (38)$$

An example of a coasting X-field with $p = n = 2.2$ and $a_c = 7$ kpc is shown in the right panel of Fig. 8.

5.3.3. Unified Halo Model

A toroidal halo field with different directions in the Northern and Southern hemisphere can be the result of differential rotation of a poloidal halo field (e.g. [Andreasen & Makarov 1988](#); [Men & Han 2003](#)). [Farrar \(2014\)](#) pointed out that – given the sign of the dipolar field discovered by [Jansson & Farrar \(2012a\)](#) – the differential rotation of the Galaxy would create toroidal halo fields with the observed directions in the Northern and Southern hemispheres. However the question of whether differential rotation can explain the observed toroidal field strength quantitatively, including its vertical and radial profiles, was not addressed. Here, we show that the toroidal field is in fact remarkably well described by the simplest possible model based on the observed differential rotation. The success of this initial simple treatment gives encouragement that a more fully developed treatment of the effects which limit the buildup of the toroidal field, can eventually enable a physics-based model of the halo field to replace the ad-hoc fitting approach which has been required up to now.

Consider a poloidal field that is dragged along with the rotation of the Galaxy and evolves via the induction equation,

$$\partial_t \mathbf{B} = \nabla \times (\mathbf{v} \times \mathbf{B}) - \underbrace{\nabla \times \eta (\nabla \times \mathbf{B})}_{\rightarrow 0 \text{ for } \sigma \rightarrow \infty}, \quad (39)$$

where the “frozen-in condition” applies for perfect conductivity, $\sigma \rightarrow \infty$, for which the magnetic diffusivity vanishes, $\eta \propto 1/\sigma \rightarrow 0$ (e.g. [Parker 1979](#)). Under these conditions and for a purely azimuthal rotation velocity v the induction equation simplifies to

$$\partial_t \mathbf{B} = \nabla \times (\mathbf{v} \times \mathbf{B}) = \begin{pmatrix} -\frac{v}{r} \partial_\phi B_r \\ \partial_z (v B_z) + \partial_r (v B_r) \\ -\frac{v}{r} \partial_\phi B_z \end{pmatrix}. \quad (40)$$

Thus, for a magnetic field that is poloidal and azimuthally symmetric at $t = 0$ ($\partial_\phi B_r = \partial_\phi B_z = 0$), the poloidal components are constant and only B_ϕ evolves with time,

$$B_\phi(t) = (B_z \partial_z v + r B_r \partial_r \omega) t, \quad (41)$$

where we introduced the angular velocity $\omega = \frac{v}{r}$ and used the solenoidality of the poloidal field.

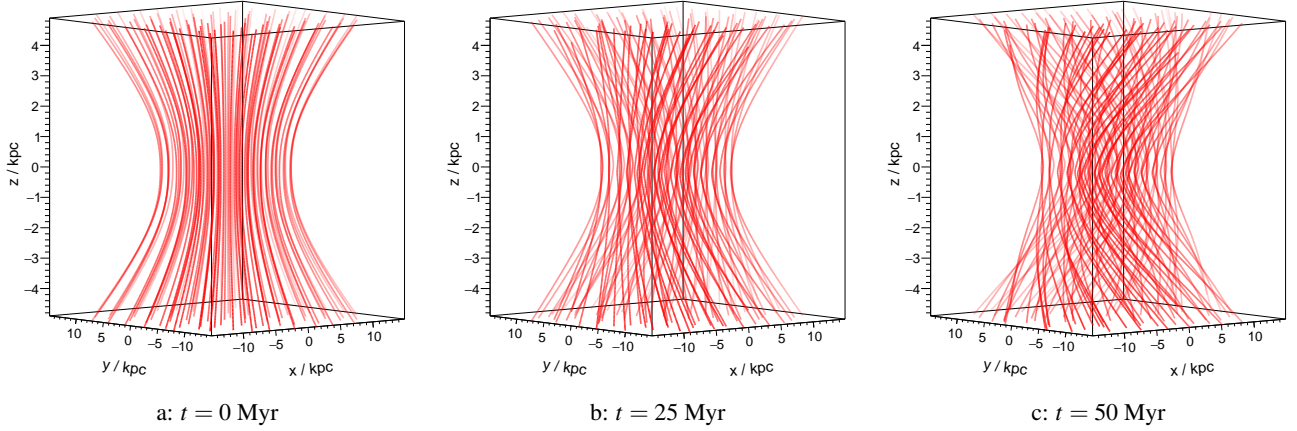


Figure 9. Illustration of the unified halo model at different times $t = 0, 15$ and 25 Myr.

Eq. (41) can be applied to evolve any type of poloidal field analytically and it describes the linear increase of B_ϕ due to the differential motion of the plasma the magnetic field is embedded in. The large-scale motion of the plasma in the Galaxy follows the Galactic rotation curve, which we take to approximately factorize as

$$v(r, z) = v_0 f(r) g(z). \quad (42)$$

Using

$$f(r) = 1 - e^{-r/r_v} \equiv f_r, \quad (43)$$

we adjust v_0 and r_v to match the velocities of high-mass star-forming regions with parallax measurements from Reid et al. (2014), leading to $v_0 = -240$ km/s (negative because the Galaxy rotates clock-wise) and $r_v = 1.6$ kpc. For the vertical velocity gradient we use

$$g(z) = 2/(1 + e^{2|z|/z_v}) \equiv g_z \quad (44)$$

with $z_v = 10$ kpc to reproduce $\partial_z v = (-22 \pm 6)$ (km/s)/kpc as measured within 100 pc of the Galactic midplane by Levine et al. (2008).¹²

With this particular choice of f_r and g_z , the evolution of the azimuthal field via Eq. (41) is

$$B_\phi(t) = (B_z \Delta_z + B_r \Delta_r) t, \quad (45)$$

with the two shear terms

$$\Delta_z = \partial_z v = -\text{sgn}(z) \frac{v_0}{z_v} f_r g_z^2 e^{2|z|/z_v} \quad (46)$$

¹²The toroidal field in the unified model is relatively insensitive to the uncertainty in $g(z)$, since the radial and vertical gradients contribute with the same sign to the twisting, contrary to the result reported in (Men & Han 2003). Terral & Ferrière (2017) explored a twisted halo model introducing a generic “winding function” $g_\phi(r, z)$ of the field lines. Their Eq. (27) is equivalent to Eq. (41) for the choice $g_\phi = t v(r, z)/r$. However, they did not investigate this explicit connection of the winding function to the velocity field $v(r, z)$ of the Galaxy, but used an ad-hoc parametric winding function.

and

$$\Delta_r = r \partial_r \omega = v_0 \left(\frac{1 - f_r}{r_v} - \frac{f_r}{r} \right) g_z. \quad (47)$$

An example of a unified halo field is shown in Fig. 9 starting at $t = 0$ with a poloidal coasting X-field with $B_p > 0$ and a logistic sigmoid cutoff at $r = 8$ kpc. Due to the radial and vertical shear of the rotation curve, Eq. (42), an azimuthal field is created at $t > 0$ that has a different sign in the Northern and Southern hemisphere to which both terms in Eq. (41) contribute constructively. Obviously, this process cannot continue in this naïve form over the lifetime of the Galaxy, or it would overproduce the observed azimuthal field strength. A steady-state azimuthal field could be obtained by including a suitable dissipative term in the induction equation and possibly a source term from the α -effect of dynamo theory (e.g. Brandenburg & Ntormousi 2023), but for the purpose of this paper we interpret the best-fit twisting time as an effective parameter of this simplest version of a unified halo model.

In summary, in this section we introduced two variants of the disk field (grand spiral or spiral spur), two variants of the poloidal field (power-function or coasting) and two variants for the toroidal halo (explicit or from twisting). These magnetic field sub-models as well as their parameters are listed in Table 1 together with a few other model parameters.

6. MODEL OPTIMIZATION

The parameters \mathbf{p} of a GMF model are optimized by minimizing the sum of the variance-weighted squared difference between the modeled m and measured d observables,

$$\chi^2 = \sum_{i=\text{RM}, Q, U} \sum_{j=1}^{N_i} \frac{(d_{ij} - m_{ij}(\mathbf{p}))^2}{\sigma_{ij}^2}, \quad (48)$$

where the second sum runs over the N_j lines of sight available for the RM and synchrotron data. Each line of sight data

Table 1. List of parameter names of different model components.

name	explanation	unit	value
disk field			
common parameters			
α	pitch angle	deg.	free
z_d	transition height	kpc	free
w_d	vertical transition width	kpc	free
a) grand-design spiral, Eqs. (11) and (10)			
B_m	magnetic field strength of mode m	μG	free
ϕ_m	phase of mode m	deg.	free
r_0	reference radius	kpc	5
r_1	inner radius	kpc	5
w_1	inner radial transition width	kpc	0.5
r_2	outer radius	kpc	20
w_2	outer radial transition width	kpc	0.5
b) spiral spur, Eq. (16)			
B_1	magnetic field strength at r_0	μG	free
ϕ_1	azimuth at r_0	deg.	free
w_S	Gaussian width	deg.	free
ϕ_c	central azimuth	deg.	free
L_c	half angular length	deg.	free
r_0	reference radius	kpc	8.2
w_c	transition width	deg.	5
toroidal halo			
a) explicit, Eq. (21)			
B_N	Northern magnetic field strength	μG	free
B_S	Southern magnetic field strength	μG	free
z_t	vertical scale height	kpc	free
r_t	transition radius	kpc	free
w_t	radial transition width	kpc	free
b) twisted, Eq. (41)			
t	twisting time	Myr	free
v_0	Galactic rotation velocity	km/s	-240
r_v	scale radius of rotation curve	kpc	1.6
z_v	scale height of rotation curve	kpc	10
poloidal halo			
common parameters			
B_p	magnetic field strength	μG	free
p	field line exponent	–	free
z_p	scale height	kpc	free
r_p	radial scale or transition radius	kpc	free
w_p	transition width	kpc	free
a) power-function, Eqs. (22) and (23)			
b) coasting, Eqs. (35) and (36)			
a_c	coasting radius	kpc	free
other model parameters			
κ	n_e - B correlation coefficient, Eq. (2)	–	free
ξ	magnetic striation factor Eq. (8)	–	free

d_{ij} is obtained by averaging available measurements over a finite solid angle around the line-of-sight direction. These

angular *pixels* are defined by the HEALPIX resolution of the data. The predicted values m_{ij} of a GMF model, $B(x; \mathbf{p})$, are given by the numerical evaluation of the line-of-sight integrals for RM, Q and U . Even for a perfect GMF model, the differences $d_{ij} - m_{ij}$ are expected to be distributed with a variance of σ_{ij}^2 , since the data is subject to experimental uncertainties and the model prediction do not include “Galactic variance” originating from random magnetic fields and from fluctuations of the densities of thermal electrons and cosmic-ray electrons. In general, Galactic variance will introduce correlations between adjacent pixels if the size of the perturbations is larger than the angular size of one pixel. In that case, the full covariance matrix needs to be included in the calculation of the χ^2 . It is, however, non-trivial to calculate the coefficients of the matrix, because one needs to know the spatial distribution of the turbulence and coherence length for the magnetic field and the thermal and cosmic-ray densities. Different approximations have been applied in previous analyses. Jaffe et al. (2010) and Adam et al. (2016) used a model of the three-dimensional random field strength with a constant coherence length and unperturbed electron densities to calculate the diagonal elements of the covariance matrix. In a more data-driven approach, one can measure the sub-pixel variance $\hat{\sigma}^2$ of the measurements within one pixel and use it as a weight in the fit. Naïvely, the average over N observations within one pixel would then reduce the fluctuations of the mean by a factor of $1/N$, but due to the aforementioned coherent effects, the effective variance will typically be larger. Based on a toy model of coherent cells along the line of sight, Pshirkov et al. (2011) suggested to use $\hat{\sigma}^2/\delta^2$ as the pixel variance, with $\delta \approx 3$, but the exact value of δ depends on the integration distance in units of coherence length over which the GMF contributes to the observations (see also (Terral & Ferrière 2017)). Keeping in mind that the overall normalization of the χ^2 could be off by a factor of δ , we follow the procedure of JF12 and simply use $\hat{\sigma}^2$ itself to weight the data points.

The best set of n model parameters \mathbf{p} are found performing a multi-dimensional optimization of Eq. (48) with the MINUIT program (James & Roos 1975) using its MIGRAD method that implements a variable metric gradient descent (Fletcher & Powell 1963; Fletcher 1970). Deterministic gradient methods like MIGRAD descend quickly to a local minimum which may not always coincide with the global minimum. To find this global optimum we use the heuristic multi-start method, i.e. we perform a number of gradient-descent minimization runs starting at different positions $\mathbf{p}_{\text{start}}$ distributed uniformly in the n -dimensional hypercube of the parameter space. The run with the smallest local χ^2 is then considered to be the global minimum. For the model fits performed in this paper we run typically $\mathcal{O}(100)$ minimizations. The fact that usually many runs from very different starting

positions converge to the same minimum local χ^2 , increases our confidence that the n -dimensional likelihood contour of the optimization problem at hand is well-behaved and that we have indeed identified the global minimum of each model variation investigated. The main advantage of this simple multi-start method is that such a repeated gradient-descent can be trivially parallelized on a computing cluster and thus it provides an efficient method to search for the global minimum of a model, since each gradient search is very fast.¹³

For each minimization run, a good first approximation of the covariance matrix of the best-fit parameters can be obtained by the parabolic estimates derived from the Hesse-matrix of the second derivatives of the χ^2 with respect to the parameters at the minimum. These estimates come without any additional computational cost, since the Hesse matrix is anyway calculated by MINUIT during the minimization. For the final fiducial models presented in Sec. 7, more precise confidence intervals of the parameters at the minimum are derived with the profile likelihood method, i.e. by finding for each parameter the two values $p_{\text{up/low}}$ at which $\chi^2(p_{\text{up/low}}) = \chi^2_{\text{min}} + m$, while marginalizing over the other $n - 1$ parameters. These estimates are obtained using the MINOS algorithm of MINUIT and each evaluation of one $p_{\text{up/low}}$ pair is about as computationally expensive as the overall minimization itself. Unless stated otherwise, we quote the 68% (“one σ ”) intervals obtained for $m = 1$.

It is worthwhile noting that our approach differs from that of previous GMF studies, which used Markov-Chain Monte Carlo (MCMC) to explore the model parameters, (e.g. Jansson et al. 2009; Jaffe et al. 2010; Jansson & Farrar 2012a; Terral & Ferrière 2017). MCMC is the preferred method to sample the posterior distribution of a model given the data, but it is not an efficient optimizer (e.g. Hogg & Foreman-Mackey 2018). Moreover, for most applications, the approximate covariance matrix and the confidence intervals derived with the profile likelihood method provide information equivalent to the MCMC samples; see, e.g. (Ade et al. 2014), for a comparison of the two methods in the context of cosmological parameter estimation. Most importantly, the ability to efficiently optimize the parameters of many different models is of paramount importance for the GMF inference, since, as will be shown in Sec. 7, the systematic differences resulting from different model assumptions are typically much larger than the precision estimated for the parameter uncertainties of a particular model.

7. RESULTS

7.1. Base Model

For the results presented in the following, we have optimized the parameters of more than 200 combinations of magnetic field models and auxiliary models to obtain an overview of the range of GMF models attainable in the full set of possible combinations.¹⁴ Many of these model variations are performed with respect to our fiducial “base” model which consists a three-mode grand-design spiral disk field, an explicit toroidal halo and a coasting X-field with a logistic sigmoid radial dependence; there is no correlation between n_e and B and the striation is a free parameter. The sky maps of RM, Q and U resulting from this model are calculated with the YMW16 thermal electron model and a cosmic-ray electron density derived for $h_D = 6$ kpc. The model parameters are adjusted to fit the data yielding an optimum with an acceptable goodness of fit of $\chi^2/\text{ndf} = 7923/6500 = 1.22$, where ndf denotes the number of degrees of freedom, i.e. the number of data points minus the number of free parameters, which is $n_{\text{par}} = 20$ in this case. The contribution from RM pixels to the χ^2 is 4354 ($n_{\text{RM}} = 2838$) and from Q and U pixels it is 3569 ($n_Q + n_U = 3682$), i.e. the model describes the polarized synchrotron data slightly better than the RMs.

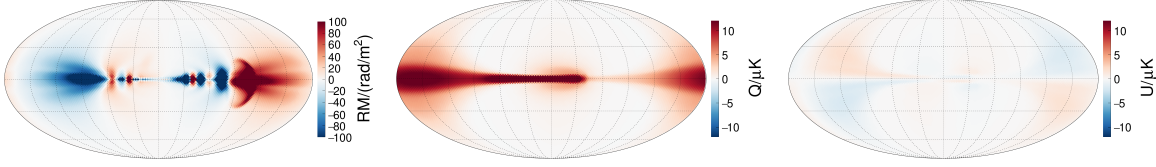
The contributions of each model component (i.e. disk field and toroidal and poloidal halo) to RM, Q and U is shown separately in the three top rows of Fig. 10 and the predicted sky maps for the sum of all components is displayed in the fourth row. Here it is interesting to see how the interplay of different model components create the large-scale features observed in data. As pointed out above, the sum of the disk and toroidal field produces the large-scale structure of RMs, see Eq. (19). The polarized intensity on the other hand, is mostly generated by the toroidal and poloidal halo. And, whereas the overall RM can be obtained by summing the RM of each component ($\text{RM} \propto B_{\parallel} = (\sum B_i)_{\parallel} = \sum B_{i\parallel}$), the sky pattern of the Stokes parameters of the full model is not the sum of its components since e.g. $Q, U \propto B_{\perp}^2 = ((\sum B_i)_{\perp})^2 \neq (\sum B_{i\perp})^2$.

The masked model, data and “pull” are shown in the three bottom rows. The pull is the difference between the data and model in units of standard deviation of the data, and the sum of all squared pulls yields the χ^2 , Eq. (48). For a perfect match of data and model, the pull should fluctuate randomly around zero with a standard-normal distribution, but here several large regions exist in which the pull has consistently negative or positive values beyond $\pm 1\sigma$. Some of these are close to masked regions, e.g. at the edges of the

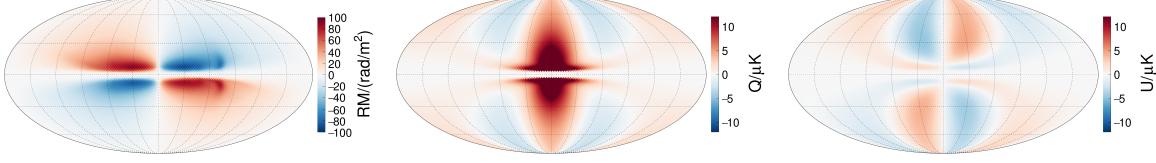
¹³The optimization of the 20-parameter base model discussed in Sec. 7 needs on average 4000 χ^2 evaluations to converge. Each evaluation takes 4 seconds on an Intel® Xeon® E5 processor at 2.4 GHz. For each evaluation, B , n_e , n_{cre} and j_V are calculated at $\mathcal{O}(10^6)$ positions throughout the Galaxy to calculate the adaptive line-of-sight integrals of RM, Q and U .

¹⁴The combination of two disk field models, eight poloidal field models, two toroidal field models, two thermal electron models, two synchrotron products and six cosmic-ray electron models, results in 1536 possible model variations.

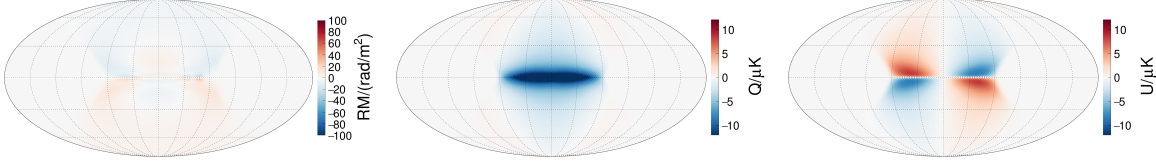
disk



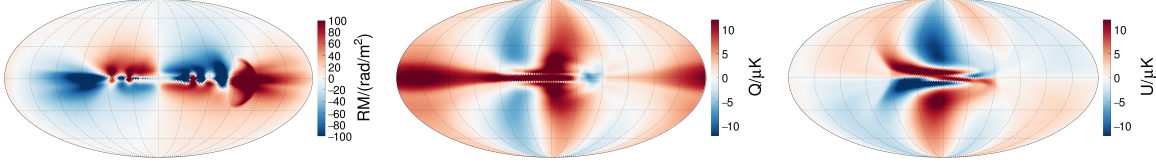
toroidal halo



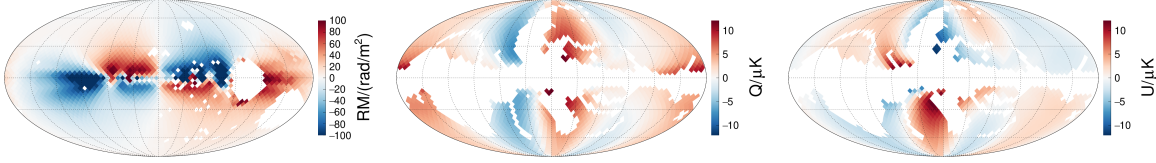
poloidal halo



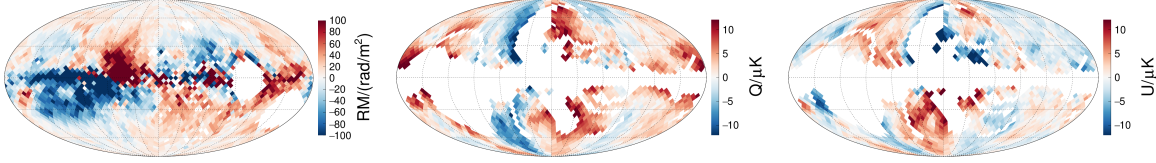
full model



masked model



data



pull

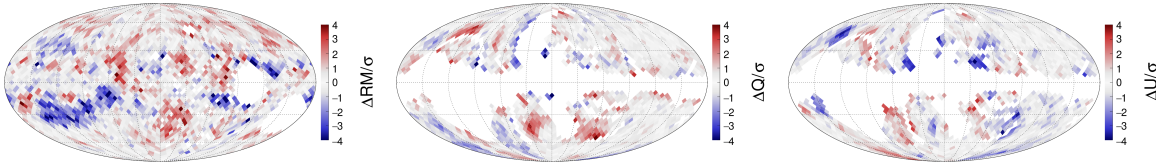
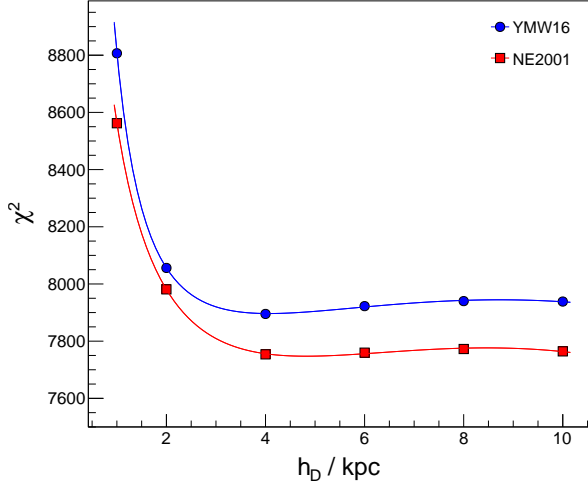
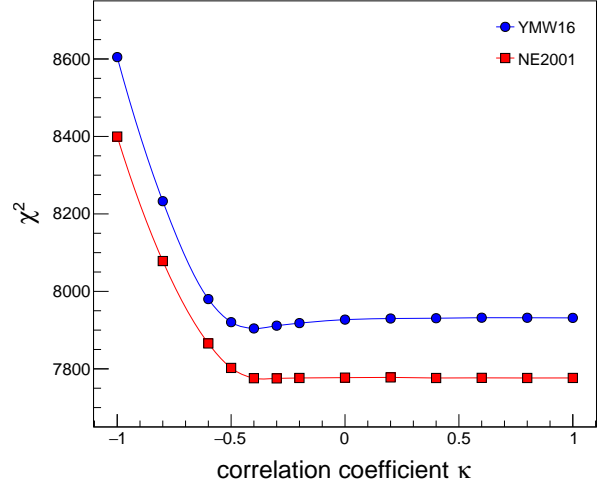
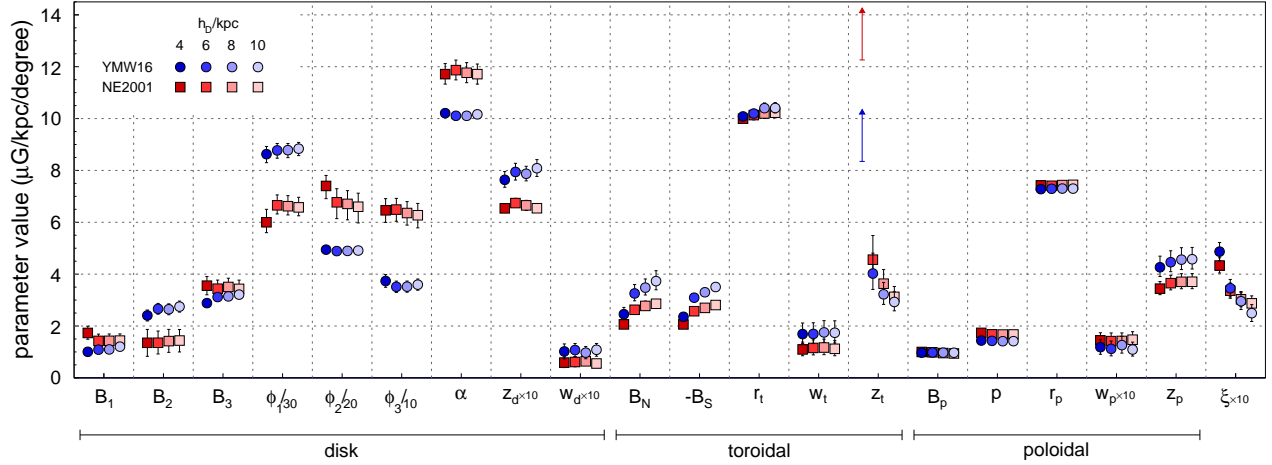


Figure 10. Data and base model prediction for RM, Q and U . The predictions from the individual model components are shown in the top rows, followed by full model prediction. The bottom three rows show the masked model, the data and the pull, i.e. the difference between model and data in units of the standard deviation of the data.

masks for the North Polar spur and loop III for Q and U and close to the mask for the Gum nebula for RM, implying a certain amount of leakage of these features beyond the mask. Others, like the large region of negative pull for RM below the Galactic plane at longitudes of $60^\circ < \ell < 150^\circ$ could indicate deficiencies in the modeling of the global structure of the GMF, e.g. an azimuthal variation of the scale height of the toroidal field. It is, however, plausible that most regions with large-scale deviations can be attributed to local pertur-

bations that appear as structures of large angular scale due to their proximity.

Apart from these potentially local structures, the base model successfully describes all the large-scale features of the data, in particular the anti-symmetric structures of the RM sky and the tilted large-scale “lobes” of negative and positive Q and U . The parameters of the base model can be found in the first column of Table 3.

a: Half-height h_D of the cosmic-ray diffusion volume.b: Correlation coefficient κ between the magnetic field and thermal electron density.**Figure 11.** Goodness of fit, Eq. (48), for two different models of the thermal electron density, NE2001 (red) and YMW16 (blue), and as a function of h_D (left) and κ (right).**Figure 12.** Best-fit parameter values of the disk, toroidal and poloidal GMF components for different values of the half-height h_D of the cosmic-ray diffusion volume, and for two different models of the thermal electron density, NE2001 (red) and YMW16 (blue). See Table 1 for a short explanation of each parameter. Some parameter values have been multiplied by a scale factor, as indicated in the axis labels, to fit in one panel with a single y-axis. One-sigma uncertainties are shown as error bars and arrows indicate the 84% CL lower limits on the parameters

7.2. Thermal and Cosmic-Ray Electrons

To study the dependence of the inferred GMF on the auxiliary models of the thermal and cosmic-ray electron density, we repeat our fits for the model variations discussed in Sec. 4. The best-fit χ^2 values for different half-heights of the cosmic-ray diffusion volume, h_D , and for the NE2001 and YMW16 model are shown in Fig. 11a. Here the functional forms for the GMF model are identical to the one used for the base model. As can be seen, the fit quality deteriorates rapidly for small values of the height of the diffusion volume

and it reaches a near-constant value at $h_D \gtrsim 4$ kpc. For small values of h_D , the decreasing vertical extent of the cosmic-ray electron halo cannot be compensated for by a larger magnetic halo.¹⁵ Interpolating between the fit results at discrete values of h_D , we estimate a 5- σ lower limit on the size of the

¹⁵For illustration, assume an exponential height dependence of n_{cre} and B with scale heights z_{cre} and z_B . Then, using Eq. (3), the height-dependence of the synchrotron emissivity is $j_v \propto e^{-|z|/z_{\text{syn}}}$ with $z_{\text{syn}} = z_{\text{cre}}/(1 + 2z_{\text{cre}}/z_B)$. It follows that for a given z_{syn} of the data, z_{cre} has to be at least $\geq z_{\text{syn}} (z_B \rightarrow \infty)$.

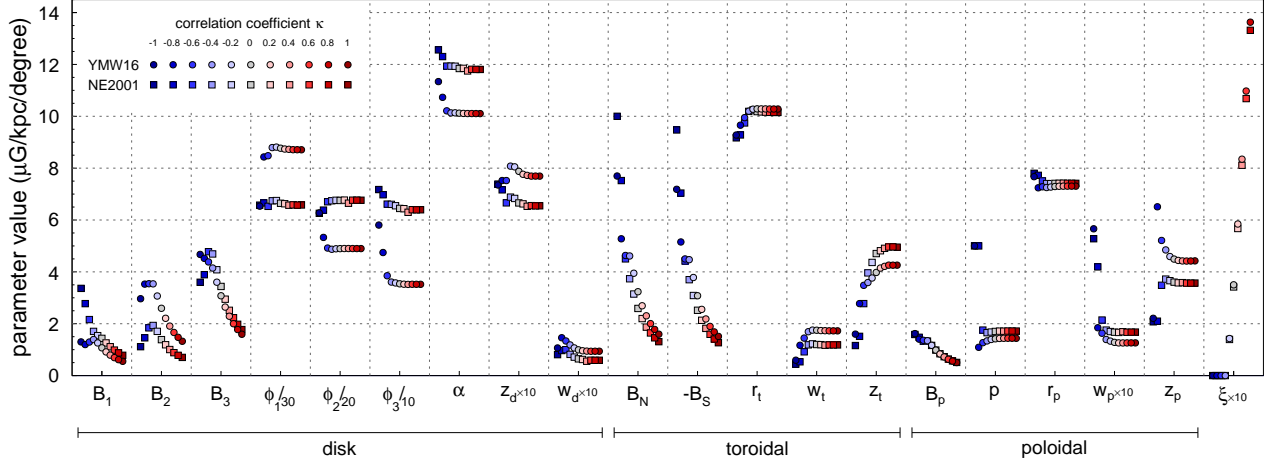


Figure 13. Best-fit parameter values of the disk, toroidal and poloidal GMF components for different values of the correlation coefficient between the magnetic field and thermal electron density κ and for two different models of the thermal electron density, NE2001 (red) and YMW16 (blue). See Tab. 1 for a short explanation of each parameter. Some parameter values have been multiplied by a scale factor, as indicated in the axis labels, to fit in one panel with a single y-axis. No parameter uncertainties are shown here, see Fig. 12.

diffusion volume of

$$h_D \geq 2.9 \text{ and } 3.5 \text{ kpc}, \quad (49)$$

where the two values correspond to the fits with NE2001 and YMW16, respectively. This lower limit is, however, only indicative since in this analysis, there is no feedback between the derived magnetic field and the propagation of cosmic-ray electrons, see Sec. 4.2.

The interplay of diffusion height and derived magnetic field parameters can be seen in Fig. 12, where the GMF model parameters of the different fits for $h_D \geq 4$ kpc are displayed. Especially the fitted scale height z_t of the toroidal field depends strongly on h_D . For $h_D = 4$ kpc only a lower limit on z_t can be estimated. In the following, we will therefore only investigate GMF models derived for n_{cre} densities within $6 \leq h_D/\text{kpc} \leq 10$, for which the best-fit values of z_t are finite and compatible with current estimates of the size of the diffusive halo estimated from the analysis of unstable secondary cosmic-ray nuclei.

Concerning the models of the density of thermal electrons in the Galaxy, it can be seen in Fig. 11a that the fits with the old NE2001 model result in a consistently better fit quality than the ones performed with the recent YMW16 model. Even though the difference is statistically significant ($\Delta\chi^2 = -167$ at $h_D = 6$) we consider both models in our analysis, since the latter n_e model gives a better description of Galactic pulsars DMs than the former. Switching between these two models has a larger systematic impact on the values of most GMF parameters than a change in h_D , see Fig. 12.

7.3. Striation or Correlation?

It is well known that the magnetic field strength derived from the observed rotation measures is smaller than the one

derived from the observed Galactic polarized synchrotron emission. One way to reconcile the two observables is to postulate the existence of an anisotropic or striated random field that fluctuates along the coherent field lines, which leads to an increase in polarized intensity without changing the rotation measures. For our base model, the best-fit value of the striation factor ξ , see Eq. (8), is

$$\xi_{\text{base}} = 0.35 \pm 0.03, \quad (50)$$

implying that the energy density in the coherent and striated field component are almost equal (energy density $u_B \propto B^2$, $B' = (1 + \xi)B$, $u_{B'}/u_B = (1 + \xi)^2 = 1.8 \pm 0.1$).

Another reason for the mismatch between magnetic fields inferred from RM and PI observations could be an anti-correlation of the thermal electrons and the magnetic field, leading to smaller Faraday rotation than in the uncorrelated case. Here we perform, to our knowledge for the first time, an analysis of RM and PI allowing for a modified RM due to an n_e - B correlation with coefficient κ , as derived by Beck et al. (2003) (cf. Sec. 2). Here we use the PLANCK-tune of the JF12 random field b (Jansson & Farrar 2012b; Adam et al. 2016) to evaluate Eq. (2) for a fixed value of b , but a coherent field B that is allowed to float freely during the fit.

The fits are performed for different values of κ and the resulting dependence of the fit quality on the correlation coefficient is displayed in Fig. 11b. As can be seen, a large anti-correlation of n_e and B is disfavored and the five-sigma lower limit is found to be

$$\kappa \geq -0.52 \text{ and } -0.49, \quad (51)$$

where the two values correspond to the fits using the NE2001 and YMW16 models of n_e , respectively. The optimal fit to the

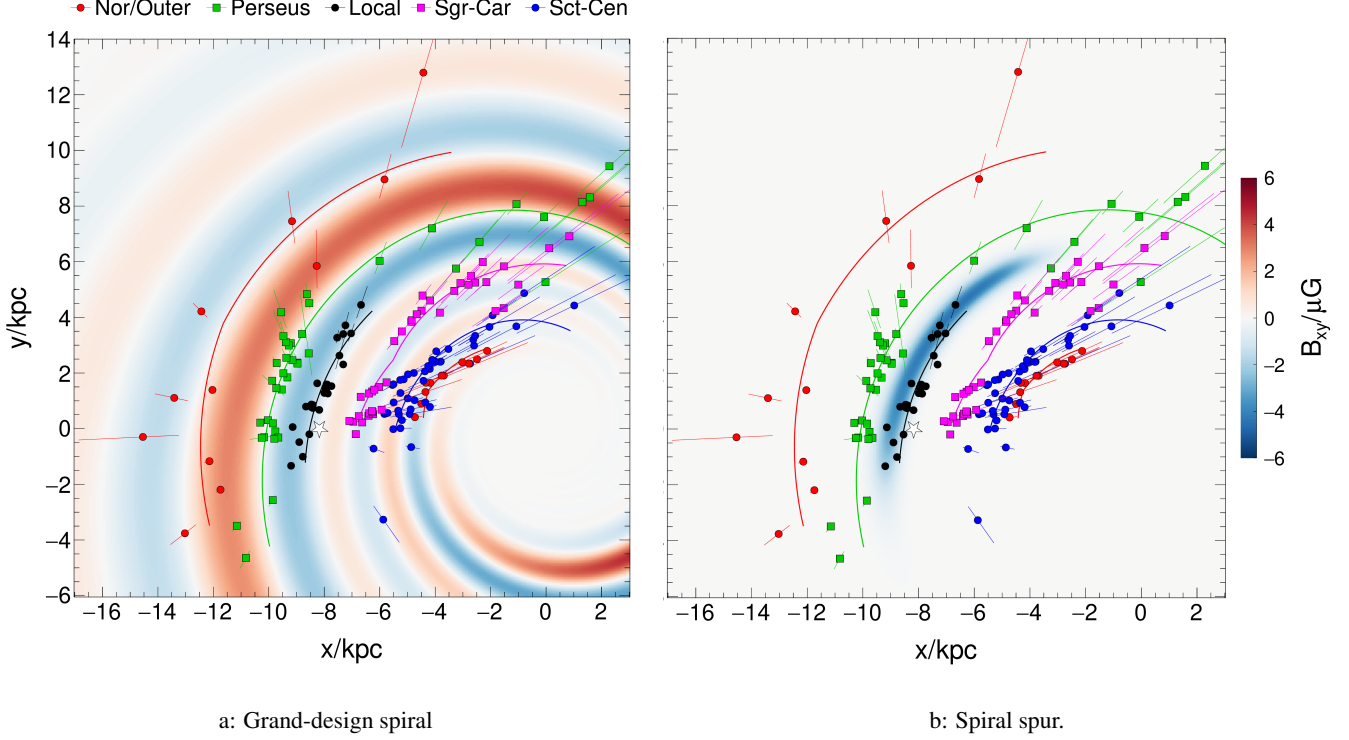


Figure 14. Magnetic field of the disk component for the grand-design spiral (left) and spiral spur (right) GMF model. The horizontal magnetic field strength in the x - y plane at $z = 0$ is displayed with colors ranging from blue (counter-clockwise field) to red (clock-wise field). Superimposed points with distance error bars are the locations of tracers of the spiral structure of the matter density of the Milky Way (high-mass star-forming regions with parallax distances) and the curved colored lines are the inferred location of spiral arm segments, both from Reid et al. (2019).

data is at $\kappa \approx -0.4$, but the χ^2 minimum is very broad and all fits above this value fit the data similarly well. The reason for this degeneracy can be understood by examining the change of fit parameters with κ , as shown in Fig. 13. Given the two degrees of freedom of rescaling the magnetic field strengths of each model component and the striation factor, it is always possible to match the RM and PI data as long as $\xi > 0$. In the following, we will not further investigate the fits with $\kappa > 0$, since our fiducial fits with $\kappa = 0$ exhibit already a large degree of striation close to equipartition with the coherent field (see above). Instead, we will concentrate on the best fit at $\kappa = -0.4$ where the striation parameter is zero as an alternative to the fiducial model. At this value of κ , the magnetic field scale is set by the PI data, whereas at $\kappa = 0$ the scale is set by the RM data. In this extreme scenario, where no striated random fields contribute to the polarized intensity and the Faraday rotation is diminished by the anti-correlation of B and n_e , the fitted magnetic field strengths (B_m , $B_{N/S}$ and B_p) are about a factor 1.4 larger than in the fiducial case.

7.4. Synchrotron Data Products

The choice of data product for the Stokes Q and U parameters affects the GMF fit due to the differences in the large-scale structure of derived sky maps, see discussion in

Sec. 3.2 and the comparisons shown in Fig. 22 in the Appendix. Moreover, and perhaps more importantly, since these differences are relatively small, different products differ by the variance of Q and U within a pixel over which we average these values. Since we use these variances as a weight of the data when optimizing Eq. 48, they also affect the outcome of the fit.

For our simple arithmetic average of the Q and U values of PLANCK and WMAP, the variance is calculated for all data points before averaging, therefore we expect it to be the arithmetic average of the PLANCK and WMAP variances plus an additional contribution from the systematic difference between the two products. On average, the variance derived from the PLANCK and COSMOGLOBE maps is about 0.8 smaller than the one of our default synchrotron map, and about the same for the WMAP data. Keeping in mind that WMAP could measure at lower frequencies where the synchrotron intensity is larger by a factor of $(22.5 \text{ GHz}/30 \text{ GHz})^{-3.1} = 2.4$, it is not clear to us to which extent the smaller variance of PLANCK (and by extension COSMOGLOBE) is actually due to an improved measurement of the synchrotron radiation or due to the use of more aggressive foreground smoothing priors in the analysis.

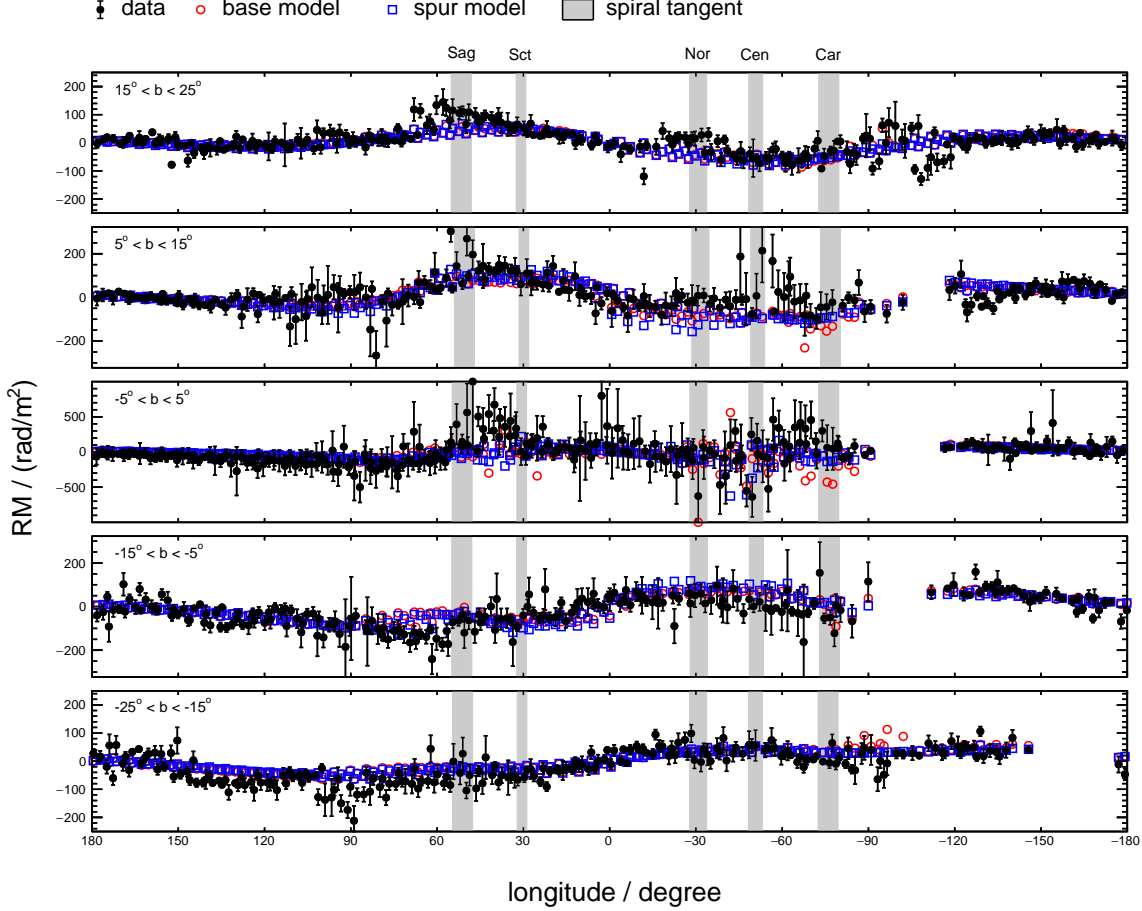


Figure 15. Comparison of data (black points with error bars) and models (red open circles: base model with a grand-design spiral disk field, blue open squares: spiral spur model) in five latitude slices around the Galactic plane. Every point is the RM value detected/predicted in one HEALPIX pixel ($N_{\text{side}} = 16$). Gray bands are drawn at the longitudes of tangent points of the spiral arms of the Galaxy. The width indicates the range of tangent positions in different observables catalogued by Vallée (2022).

As a consequence of smaller variances, the fits using PLANCK and COSMOGLOBE have a χ^2 that is worse than the one of the base model by a factor of 1.4 and 1.2, respectively. We have checked that the worse fit is indeed mostly due to the different variances (and not the different values of Q and U), by performing a fit of the PLANCK data with our default variances, in which case the fit quality was only worse by a factor of 1.03.

The GMF models obtained with alternative data products are qualitatively similar, but the parameters obtained in these fits differ from the one of the base model. The differences are mostly not driven by the systematic differences between the sky maps, but rather caused by the larger relative “pull” on the χ^2 of Q and U data with respect RM data. The sensitivity of the parameter values on the data-driven weights are intrinsic to the method used in this analysis and needs to be considered when estimating the GMF model uncertainties, see Sec. 7.8 below.

7.5. Disk Field

7.5.1. Grand-Design Spiral

Many of the previous attempts to model the global structure of the disk field enforced a certain number of “magnetic arms”, often following the inferred large-scale structure of matter density in the Galaxy. Due to our more flexible decomposition of the spiral field into azimuthal Fourier modes, we can let the data decide how much spiral structure is needed. We have fit the RM and PI data using a different number of Fourier modes ranging from 1 to 5. As expected, the fit quality continuously improves with the number of modes n_{mode} , since each adds two more free parameters (amplitude and phase) to the fit. Using Wilks’ theorem (Wilks 1938), we find that the improvements of the fit quality of the base model are significant up to $n_{\text{mode}} = 3$, with a $\Delta\chi^2 = 153.2$ going from 2 to 3 modes and $\Delta\chi^2 = 12.7$ from 3 to 4 modes. The same conclusion is reached using the Bayesian information criterion, $\text{BIC} = \chi^2 + n_{\text{par}} \ln(n_{\text{data}})$

(Schwarz 1978), which is minimal at $n_{\text{mode}} = 3$. We have also tested that the required number of modes remains three when changing the height of the diffusion volume, h_D , used to calculate n_{cre} and when using a twisted X-field.

Three azimuthal modes correspond to six “magnetic arms” of alternating polarity. The grand-design configuration of our neCL fit variant (using the NE2001 thermal electron model) has already been shown above in the right panel of Fig. 7. The best-fit disk field of the base model is displayed in the left panel of Fig. 14, where we also show the location of tracers of the spiral structure of the matter density of the Milky Way, given here by the measurements of trigonometric parallaxes of high-mass star forming regions from Reid et al. (2019). As can be seen, we find a remarkable alignment of the fitted magnetic spiral structure and these tracers. Large coherent field strengths are present in the interarm regions, but the coherent field strength is close to zero at the location of the spiral matter segments derived by Reid et al. (2019), shown as lines in Fig. 14. This result is similar to what is observed in external galaxies, where the strongest ordered fields are detected in the interarm regions (Beck 2016).

The fitted pitch angle, α , of the disk field is found to be nearly independent of the assumed cosmic-ray halo size, n_e - B correlation coefficient ($\kappa \geq -0.4$) and functional form of the magnetic halo. However, the fits with different models of the thermal electron density result in pitch angles that are systematically different with respect to each other by $\pm 1^\circ$, see Fig. 12. The average of the value obtained using the NE2001 and YMW16 thermal electron models is

$$\alpha = (11.0 \pm 0.3 \text{ (stat.)} \pm 1.0 \text{ (} n_e \text{)})^\circ. \quad (52)$$

This value is in good agreement with the pitch angle of the local (Orion–Cygnus) spiral arm of $(11.4 \pm 1.9)^\circ$ (Reid et al. 2019) and the pitch angles of $\alpha = (9.87 \dots 11.43)^\circ$ of the grand-design logarithmic spiral model fitted by Hou & Han (2014) using HII regions as spiral tracers. Thus, the pitch angles of the spiral structure of the magnetic field and the matter density in the Milky Way are about equal, similar to what is observed for external spiral galaxies (Van Eck et al. 2015).

7.5.2. Local Spur

What drives the fit of the grand-design spiral disk field? Is it the RM values at longitudes where the line of sight is tangential to a spiral arm? These magnetic tangents are clearly visible in the predicted RMs in the top left plot of Fig. 10, but they are not so obvious in the RM of the data, possibly due to the large variance present in the data at low latitudes. Alternatively, the fit of the disk field might be mostly determined by the large-scale “butterfly pattern” of RMs, see Eq. (19), and therefore mostly from the disk field in the vicinity of the Sun.

To test this possibility, we fit the data without a grand-design magnetic pattern, but include only one local magnetic spur, as introduced in Sec. 5.2.3. The fitted pitch angle of the local spur is $(12.1 \pm 0.6)^\circ$ and does not depend on the thermal electron model used. The best-fit local spur is displayed in the right panel of Fig. 14. It is located at the edge of the local Orion–Cygnus spur and has a magnetic field strength of $4.30 \mu\text{G}$ at the reference radius of 8.2 kpc. The quality of this fit is found to be slightly worse than the one of the base model (7991 instead of 7923), but close enough to conclude that both models are approximately equivalent.

For a closer look at the differences between the spur and base model, we show the RM values in bands of latitude for data and the two models in Fig. 15. As can be seen, both models give the same overall good description of the longitude-dependence of RM of the data. The base model (shown as red open circles) exhibits distinct RM features at low latitudes, shown in the middle panel for $|b| < 5^\circ$, but none of these are visible in the data.

The near-equivalence of these two radically different disk field models is a consequence of the fact that the extragalactic RMs used in the fit constrain only the integrated Faraday rotation to the edge of the Galaxy. The model degeneracy could, in principle, be broken by including RMs from Galactic pulsars into the fit to provide cumulative RMs at different distances. However, pulsar RMs are currently of limited use, since the distances to most pulsars are not known with sufficient precision. Some previous GMF studies used the “DM-distance” (i.e. the distance d at which $\text{DM}' = \int_0^d n_e(x(r)) dr$ equals the observed DM) to calculate the model RMs, but this introduces an additional dependence on thermal electron density models which is difficult to account for in the GMF model optimization. Notwithstanding these caveats, it is interesting to note that Han et al. (2018) derived a six-arm grand-design spiral model from the RMs of pulsars and extragalactic sources, which is qualitatively very similar to the disk field of our base model. More studies are however needed to unequivocally prove the existence of a grand-design magnetic spiral in our Galaxy. Until then, a conservative approach is to consider the two models introduced in this section as extreme possibilities for the coherent magnetic field in the disk of the Milky Way.

7.6. Poloidal Field

We begin by reassessing the need for a poloidal component to describe the data, performing a fit without including such a component. The resulting fit quality deteriorates tremendously, by $\Delta\chi^2 > +2100$ with respect to the base model, irrespective of the thermal electron model used in the fit. As can be seen in Fig. 10, the poloidal component contributes only little to the RMs. However it would be incorrect to con-

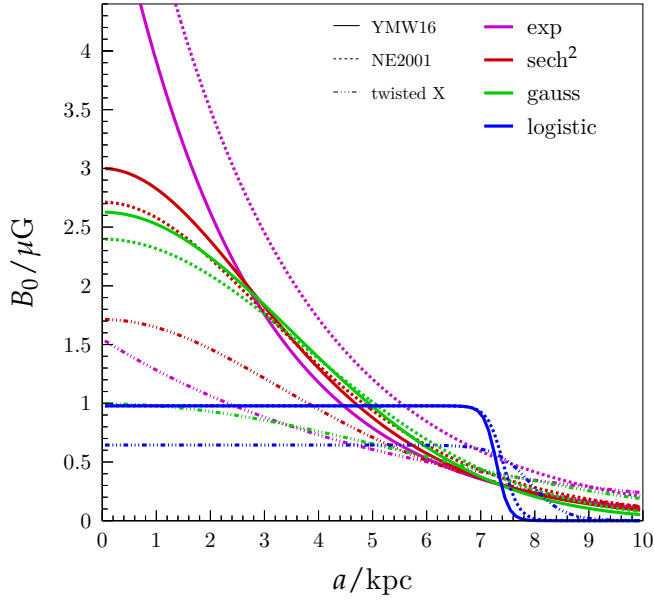


Figure 16. Best-fit radial dependence of the z -component of the poloidal magnetic field at $z = 0$, $B_0(a)$, see Eqs. (22) and (23). Different radial functions are shown in different colors, see Eqs. (29) - (32). Variations in the thermal electron density and toroidal field type used during the fit are shown with different line styles, as indicated in the figure legend.

clude that the fit cannot determine whether the X-field is coherent or striated, since the Stokes parameters of the model components do not add linearly (see discussion in Sec. 7.1). In fact, if a striated X-field were equivalent to a coherent one, then the fit quality would only depend on the orientation, but not the direction of the coherent X-field, but the $\Delta\chi^2$ is +8679, when reversing the direction of the X-field.

We also tried to fit the data with a N-S reflection-symmetric X-field (characteristic of a S1 dynamo), instead of a dipolar one (A0 dynamo), however the fit is much worse ($\Delta\chi^2 > +1700$). Furthermore, we checked for the base model if different strengths of the magnetic field normalization B_p in the Northern and Southern hemisphere are preferred by the data. A different value in the two hemispheres would be required by flux conservation if there were a net inward or outward flux in the disk in an $m = 0$ mode. We find that any such asymmetry must be small, since the difference of the fitted values for the two hemispheres is $\Delta B_p = (0.12 \pm 0.07) \mu\text{G}$.

Inspecting the pixel-by-pixel contributions to the χ^2 we find that the poloidal fit is mainly driven by the Q and U data at longitudes $|\ell| < 60^\circ$. Unless a very peculiar¹⁶ foreground

¹⁶We performed a few initial tests with a magnetic field compressed at the edge of a local foreground bubble (e.g. Ferriere et al. 1991) using a simple spherical model with magnetic flux conservation, but could not find a configuration that described the data. More systematic studies are needed to definitively exclude this possibility; see also (Pakmor et al. 2018).

is responsible for these large-scale features in Q and U , we confirm with high significance the conclusions of Jansson & Farrar (2012a) that the polarized synchrotron intensity cannot be described without the presence of a dipolar X-field in the Galaxy.

We find that the data is described equally well by a power-function and a coasting X-field ($\chi^2 = 7926$ and 7923 , respectively), since the major differences between the field lines of the two models are at large radii, where the field is small, see Fig. 8. There is, however, a clear preference regarding the choice of the radial dependence of the mid-plane vertical field, Eqs. (29)-(32). The best fit to the data is obtained for the logistic sigmoid function, i.e. for a vertical field strength that is constant with galacto-centric radius and then vanishes to zero at a certain radius r_p with a transition width w_p . The tested alternatives of a Gaussian, hyperbolic secant or exponential radial dependence result in fits which are worse by $\Delta\chi^2 = +370$, $+452$ and $+508$. This clear preference for a logistic radial cutoff remains for all model variations tested (power-function or coasting X-field, twisted X-field and using different thermal electron models).

The improvement of χ^2 when using a logistic instead of an exponential function originates mostly from the RM ($\Delta\chi_{\text{RM}}^2 = 315$) and Q data ($\Delta\chi_Q^2 = 155$ and only to a lesser extent from the U data ($\Delta\chi_U^2 = 36$). Much of the improvement in χ_{RM}^2 is concentrated in one swathe of the RM sky located at $\ell \approx (-30 \pm 15)^\circ$ and $90^\circ < b < 150^\circ$ and most of the decrease in χ_Q^2 is due to a better description of the data at $15^\circ < \ell < 30^\circ$ and $b > 0^\circ$. Since we cannot be certain that these features at intermediate angular scales are global, we conservatively keep the exponential radial function as an extreme variation in our model ensemble.

The best-fit mid-plane poloidal magnetic field strengths, derived for different radial functions, are shown in Fig. 16. The largest differences of $B_0(a)$ are at small radii, $a \lesssim 4$ kpc, where the fit of the poloidal field strength is unconstrained due to the large amount of Q and U pixels masked at $|\ell| < 30^\circ$. The logistic model used in our base model has a mid-plane vertical field strength of $B_p = (0.98 \pm 0.03) \mu\text{G}$ and cuts off inside the solar circle at $r_p = (7.29 \pm 0.06)$ kpc with a transition width of $w_p = (0.112 \pm 0.029)$ kpc. In the case of the twisted X-field model, the transition is fitted to be at a somewhat large radius and the transition is broader ($r_p \sim 7.9$ kpc, $w_p \sim 0.3$ kpc). The expX model leads to a large vertical magnetic field at the Galactic Center, $B_p = (5.8 \pm 0.4) \mu\text{G}$ that falls off exponentially with scale length of $r_p = (2.5 \pm 0.1)$ kpc. For comparison, the poloidal field of the JF12 model is of similar strength with $B_p = (4.6 \pm 0.3) \mu\text{G}$ and $r_p = (2.9 \pm 0.1)$ kpc.

Thus, the expX and base models bracket the possible range of the radial dependence of the strength of the poloidal field. The corresponding uncertainty of the GMF, quantified

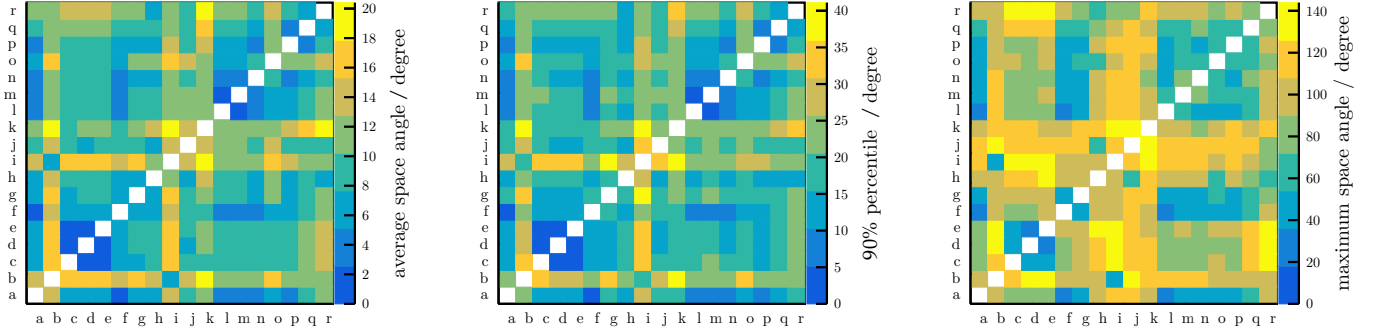


Figure 17. Comparison of models $i = a-r$ and $j = a-r$ (see Table 2) using the space angle $\theta_{ijk} = \arccos(\mathbf{u}_{ik}, \mathbf{u}_{jk})$ between the direction of charged particles ($\mathcal{R} = 1 \times 10^{19}$ V) back-tracked to the edge of the Galaxy analyzed for skymaps of arrival directions k at Earth with a resolution of $N_{\text{side}} = 32$. *Left:* average θ , *middle:* 90% percentile of θ distribution, *right:* maximum θ .

here for the first time, must be taken into account when interpreting the arrival directions of ultrahigh-energy cosmic rays and when discussing the radial dependence of cosmic-ray energy spectra derived from gamma-ray observations (e.g. Gabici et al. 2019). A better understanding of the polarized foregrounds is needed to be able to further constrain the GMF fits by including PI data towards the Galactic center.

7.7. Toroidal Field

Fitting for an “explicit” toroidal halo field, we obtain a radial extent of $r_t = (10.2 \pm 0.2)$ kpc and a vertical scale height of $z_t = (4.0 \pm 0.7)$ kpc within our base model. The estimate of the radial extent of the halo is very stable with respect to any of the model variations we have studied. The vertical scale is less certain, ranging from 2.9 to 6.1 kpc, where the lowest value is obtained assuming a large cosmic-ray diffusion volume with $h_D = 10$ kpc.

The magnitude of azimuthal field strength in the Northern and Southern hemispheres was found to vary between about 2 and 5 μG , depending on the model variation under study. For the base model, the best-fit values are $B_N = 3.3 \pm 0.3$ μG and $B_S = -3.1 \pm 0.3$ μG . In all the studied variations, the magnitude of the Northern and Southern magnetic field strength is found to be compatible within the estimated uncertainties,

$$B_N = -B_S, \quad (53)$$

which strongly suggests a common origin of the toroidal field in the two hemispheres.

Our twisted X-field model naturally explains this equality, since the magnetic field in both hemispheres originates from the shearing caused by the same velocity field. However, the fit quality of *twistX* is considerably worse than the one of the explicit fit, $\Delta\chi^2 = +462$. On a technical level, this can be due to the freedom of two different radial cutoffs values, r_p and r_t , for the toroidal and poloidal components that are available in the fit with an explicit toroidal halo. A future implementation of the unified halo model, in which a physically motivated model limits the build-up of the toroidal field,

could introduce additional radial and vertical dependencies to the amount of twist and hence result in a potentially even better description of the halo field.

A practical virtue of the unified halo model is that its built-in connection between the radial extent of the poloidal and toroidal components should make it less prone to over-fitting local structures in the data. In that case, a fitted common radial scale with a large transition width (see the dash-dotted blue line in Fig. 16) might prove to be a more accurate description of the global structure of the GMF.

In summary, the unified halo model describes the data very well using only 6 free parameters for the halo, instead of the 10 parameters needed for the base model. This is the first quantitative demonstration of earlier conjectures, that the toroidal halo of the Milky Way likely arose dynamically from differential rotation.

7.8. Model Ensemble

Based on the results presented in the previous sections, we compiled a list of viable GMF variations in Table 2. Here we already pre-selected models with $h_D \geq 6$ kpc, see Sec. 7.2, and used only the most extreme n_e - B anti-correlation of $\kappa = -0.4$, see Sec. 7.3. This leads to 18 GMF models, consisting of 7 variations of the parametric models, three variations using NE2001 rather than YMW16, one variation including an n_e - B anti-correlation, three fits with different cosmic-ray electron models and four fits with different synchrotron products.

How different are these 18 GMF models from each other? One possible way to measure the model differences is to study the motion of charged particles in the respective models and to calculate the space-angle difference in their direction after traversing the Galaxy. We performed such comparisons for many particles (rigidity $\mathcal{R} = 10^{19}$ V) starting in different directions from Earth and determined the average deflection difference, its 90% quantile and the maximum difference for each model combination. The result is shown in Fig. 17. Based on these model-to-model comparisons we can further narrow down the most important variations that encompass

Table 2. Pre-selection of model variations (GD: grand-design spiral, LS: local spur, CX: coasting X-field, PF: power function, OS13: (Orlando & Strong 2013), DPD: DRAGON plain diffusion, W: WMAP, P: PLANCK, CG: COSMOGLOBE). The last column gives the name assigned to the 8 members of the final GMF ensemble, introduced in Sec. 7.8.

id	disk	halo		n_e model	κ	n_{cre} model	h	QU	χ^2/ndf	model name
		toroidal	poloidal							
Parametric models										
a	GD	explicit	CX-sigm	YMW16	0	DPD	6	(W+P)/2	7923 / 6500 = 1.22	base
b	GD	twisted	CX-sigm	YMW16	0	DPD	6	(W+P)/2	8324 / 6504 = 1.28	
c	GD	explicit	CX-gauss	YMW16	0	DPD	6	(W+P)/2	8298 / 6500 = 1.28	
d	GD	explicit	CX-sech2	YMW16	0	DPD	6	(W+P)/2	8381 / 6500 = 1.29	expX
e	GD	explicit	CX-expo	YMW16	0	DPD	6	(W+P)/2	8431 / 6500 = 1.30	
f	GD	explicit	PF-sigm	YMW16	0	DPD	6	(W+P)/2	7926 / 6500 = 1.22	
g	LS	explicit	CX-sigm	YMW16	0	DPD	6	(W+P)/2	7991 / 6501 = 1.23	
Thermal electrons										
h	GD	explicit	CX-sigm	NE2001	0	DPD	6	(W+P)/2	7759 / 6500 = 1.19	neCL
i	GD	twisted	CX-sigm	NE2001	0	DPD	6	(W+P)/2	8221 / 6504 = 1.26	twistX
j	GD	explicit	CX-gauss	NE2001	0	DPD	6	(W+P)/2	8079 / 6500 = 1.24	nebCor
k	GD	explicit	CX-sigm	YMW16	-0.4	DPD	6	(W+P)/2	7905 / 6500 = 1.22	
Cosmic-ray electrons										
l	GD	explicit	CX-sigm	YMW16	0	DPD	8	(W+P)/2	7940 / 6500 = 1.22	cre10
m	GD	explicit	CX-sigm	YMW16	0	DPD	10	(W+P)/2	7939 / 6500 = 1.22	
n	GD	explicit	CX-sigm	YMW16	0	OS13	10	(W+P)/2	7965 / 6500 = 1.23	
Synchrotron Data Product										
o	GD	explicit	CX-sigm	YMW16	0	DPD	6	P	11013 / 6500 = 1.69	synCG
p	GD	explicit	CX-sigm	YMW16	0	DPD	6	W	8845 / 6500 = 1.36	
q	GD	explicit	CX-sigm	YMW16	0	DPD	6	CG	9758 / 6500 = 1.50	
r	GD	explicit	CX-sigm	NE2001	0	DPD	6	CG	9551 / 6500 = 1.47	

the GMF uncertainties. For instance, it can be seen that of the four models with different synchrotron products, (a, o, p, q), the COSMOGLOBE model (q) differs the most from the base model (a). The difference is similar when comparing the combination of NE2001 and COSMOGLOBE (q) to NE2001 with default synchrotron (h).

Similar comparisons lead us to select the set of eight GMF models, identified by the model acronym name in the last column of Table 2. The parameters of the eight members of this final GMF model ensemble are given in Table 3 and their properties can be summarized as follows:

- **base** is tuned to the data using the YMW16 thermal electron model and a cosmic-ray electron model calculated for a diffusion volume with a half-height of 6 kpc. The parametric model of the GMF is the sum of a spiral disk field, an explicit toroidal halo and a coasting poloidal X-field,
- **expX** uses an exponential dependence of the mid-plane vertical poloidal field instead of the default logistic radial cutoff,

- **spur** reduces the grand-design spiral disk field to a single local spur (Orion arm),
- **neCL** replaces thermal electron model YMW16 by NE2001 of Cordes & Lazio (2002),
- **twistX** has a 'twisted X-field' resulting from a unified model of the toroidal and poloidal halo,
- **nebCor** assumes an anti-correlation between the thermal electron density and the magnetic field strength,
- **cre10** uses a cosmic-ray electron model in which the half-height of the diffusion halo is increased to 10 kpc, and
- **synCG** swaps the default synchrotron product for the estimate from the COSMOGLOBE analysis.

The total energy of the coherent magnetic field within a 20 kpc radius in these eight models, respectively, is $\{1.3, 1.5, 1.2, 1.2, 0.6, 2.3, 1.2, 1.0\} \times 10^{55}$ erg. For the base model, for instance, the disk, poloidal, and toroidal components contribute $\{0.28, 0.26, 0.75\} \times 10^{55}$ erg to the total.

8. APPLICATIONS

Each of the eight GMF model variations introduced in the previous section can be considered viable estimates of the

Table 3. Parameter values and uncertainties for the eight GMF model variations. See Table 1 for a description of the parameters and Table 2 for the definition of each model variation.

name	base	expX	spur	neCL	twistX	nebCor	synCG	cre10	unit
disk field									
α	10.11 ± 0.13	10.03 ± 0.13	12.1 ± 0.6	11.9 ± 0.4	12.1 ± 0.4	10.15 ± 0.14	9.90 ± 0.13	10.16 ± 0.13	deg.
z_d	0.794 ± 0.032	0.715 ± 0.024	0.750 ± 0.027	0.674 ± 0.018	0.94 ± 0.05	0.812 ± 0.027	0.622 ± 0.018	0.808 ± 0.033	kpc
w_d	0.107 ± 0.026	0.099 ± 0.023	0.123 ± 0.024	0.061 ± 0.020	0.29 ± 0.07	0.119 ± 0.025	0.067 ± 0.018	0.108 ± 0.025	kpc
B_1	1.09 ± 0.14	0.99 ± 0.15	-4.30 ± 0.18	1.43 ± 0.26	1.37 ± 0.17	1.41 ± 0.19	0.81 ± 0.12	1.20 ± 0.14	μG
B_2	2.66 ± 0.21	2.18 ± 0.22	–	1.4 ± 0.4	2.01 ± 0.30	3.53 ± 0.27	2.06 ± 0.20	2.75 ± 0.21	μG
B_3	3.12 ± 0.15	3.12 ± 0.16	–	3.44 ± 0.34	1.52 ± 0.26	4.13 ± 0.21	2.94 ± 0.14	3.21 ± 0.15	μG
ϕ_1	263 ± 9	247 ± 10	155.9 ± 1.4	200 ± 11	236 ± 11	264 ± 8	230 ± 13	265 ± 8	deg.
ϕ_2	97.8 ± 2.8	98.6 ± 3.2	–	135 ± 12	102 ± 10	97.6 ± 3.2	97.4 ± 3.3	98.2 ± 2.8	deg.
ϕ_3	35.1 ± 2.2	34.9 ± 2.4	–	65 ± 4	56 ± 6	36.4 ± 2.5	32.9 ± 2.4	35.9 ± 2.2	deg.
w_S	–	–	10.3 ± 0.6	–	–	–	–	–	deg.
ϕ_c	–	–	157.2 ± 3.0	–	–	–	–	–	deg.
L_c	–	–	31.8 ± 3.0	–	–	–	–	–	deg.
toroidal halo									
B_N	3.26 ± 0.31	2.71 ± 0.19	2.93 ± 0.23	2.63 ± 0.17	–	4.6 ± 0.4	2.40 ± 0.12	3.7 ± 0.4	μG
B_S	-3.09 ± 0.30	-2.57 ± 0.18	-2.60 ± 0.21	-2.57 ± 0.17	–	-4.5 ± 0.4	-2.09 ± 0.11	-3.50 ± 0.35	μG
z_t	4.0 ± 0.7	5.5 ± 0.9	6.1 ± 1.4	4.6 ± 0.8	–	3.6 ± 0.6	5.6 ± 0.8	2.9 ± 0.4	kpc
r_t	10.19 ± 0.17	10.13 ± 0.19	9.75 ± 0.13	10.13 ± 0.20	–	10.21 ± 0.17	9.42 ± 0.08	10.41 ± 0.20	kpc
w_t	1.7 ± 0.4	2.1 ± 0.6	1.42 ± 0.30	1.15 ± 0.29	–	1.7 ± 0.4	0.92 ± 0.16	1.7 ± 0.4	kpc
t	–	–	–	–	54.7 ± 1.1	–	–	–	Myr
poloidal halo									
B_p	0.978 ± 0.033	5.8 ± 0.4	0.99 ± 0.04	0.984 ± 0.031	0.628 ± 0.020	1.35 ± 0.04	0.809 ± 0.024	0.969 ± 0.034	μG
p	1.43 ± 0.09	1.95 ± 0.14	1.40 ± 0.09	1.68 ± 0.11	2.33 ± 0.10	1.34 ± 0.10	1.58 ± 0.09	1.42 ± 0.09	–
z_p	4.5 ± 0.4	2.37 ± 0.22	4.5 ± 0.4	3.65 ± 0.28	2.63 ± 0.10	4.8 ± 0.5	3.53 ± 0.24	4.6 ± 0.4	kpc
r_p	7.29 ± 0.06	2.50 ± 0.07	7.20 ± 0.06	7.41 ± 0.05	7.92 ± 0.04	7.25 ± 0.07	7.46 ± 0.05	7.30 ± 0.06	kpc
w_p	0.112 ± 0.029	–	0.123 ± 0.034	0.142 ± 0.030	0.291 ± 0.035	0.143 ± 0.033	0.150 ± 0.022	0.109 ± 0.027	kpc
a_c	–	6.2 ± 0.8	–	–	–	–	–	–	kpc
other model parameters									
κ	0	0	0	0	0	–0.4	0	0	–
ξ	0.346 ± 0.034	0.51 ± 0.04	0.330 ± 0.033	0.336 ± 0.029	0.78 ± 0.04	0	0.63 ± 0.04	0.250 ± 0.033	–

GMF given the current RM, Q and U data, and the differences between the models can be regarded as an estimate of the uncertainty of our knowledge of the magnetic field of the Galaxy.

In this section, we discuss two applications in which we propagate the uncertainties of the GMF to uncertainties in the deflection of ultrahigh-energy cosmic rays and in the conversion probability of axions the Galactic magnetic field.

8.1. Cosmic-Ray Deflections

Given the arrival direction \boldsymbol{v} of an ultrahigh-energy cosmic-ray particle at Earth, the knowledge of the GMF can be used to infer its arrival direction at the edge of the Galaxy \boldsymbol{u} . In Fig. 18 we show sky maps of the *deflection angle* $\theta_{\text{def}} = \arccos(\boldsymbol{u}\boldsymbol{v})$ for each of the eight models and the JF12 model at a particle rigidity of 20 EV (1 EV = 10^{18} V). These were obtained by numerically integrating (Cash & Karp 1990; Argyro et al. 2007) the equation of motion of a negatively¹⁷

charged particle in the Galactic magnetic field until it leaves the Galaxy at a galactocentric radius of $r_{\text{max}} = 30$ kpc. The magnitude of the deflection angle is indicated by colors at each of the starting directions \boldsymbol{v} on a HEALPIX grid with $N_{\text{side}} = 64$, and the direction of the deflection is indicated by an arrow for a subset of directions on a $N_{\text{side}} = 16$ grid if $\theta_{\text{def}} > 1^\circ$. As can be seen, all eight models exhibit qualitatively similar deflection pattern but with quantitative differences as to be expected from the results presented in the last section. For instance, the nebCor model has the largest deflections because in this model the magnetic field scale is set by the polarized synchrotron data, not by the RMs. And as expected, the expX model has the largest deflections for trajectories close to the Galactic center where it has a six times larger poloidal field strength than the base model. All models exhibit a left-right asymmetry with deflections being larger if the particle is back-tracked towards positive longitudes and smaller for negative longitudes. This is the consequence of the twisted nature of the halo field.

For a closer look at the differences between the models, we show the back-tracked directions \boldsymbol{u} in Fig. 19 for a small set of arrival directions \boldsymbol{v} . The particle rigidity is again 20 EV

¹⁷The back-tracking a negatively charged test particle yields the forward trajectory of a positively charged cosmic ray.

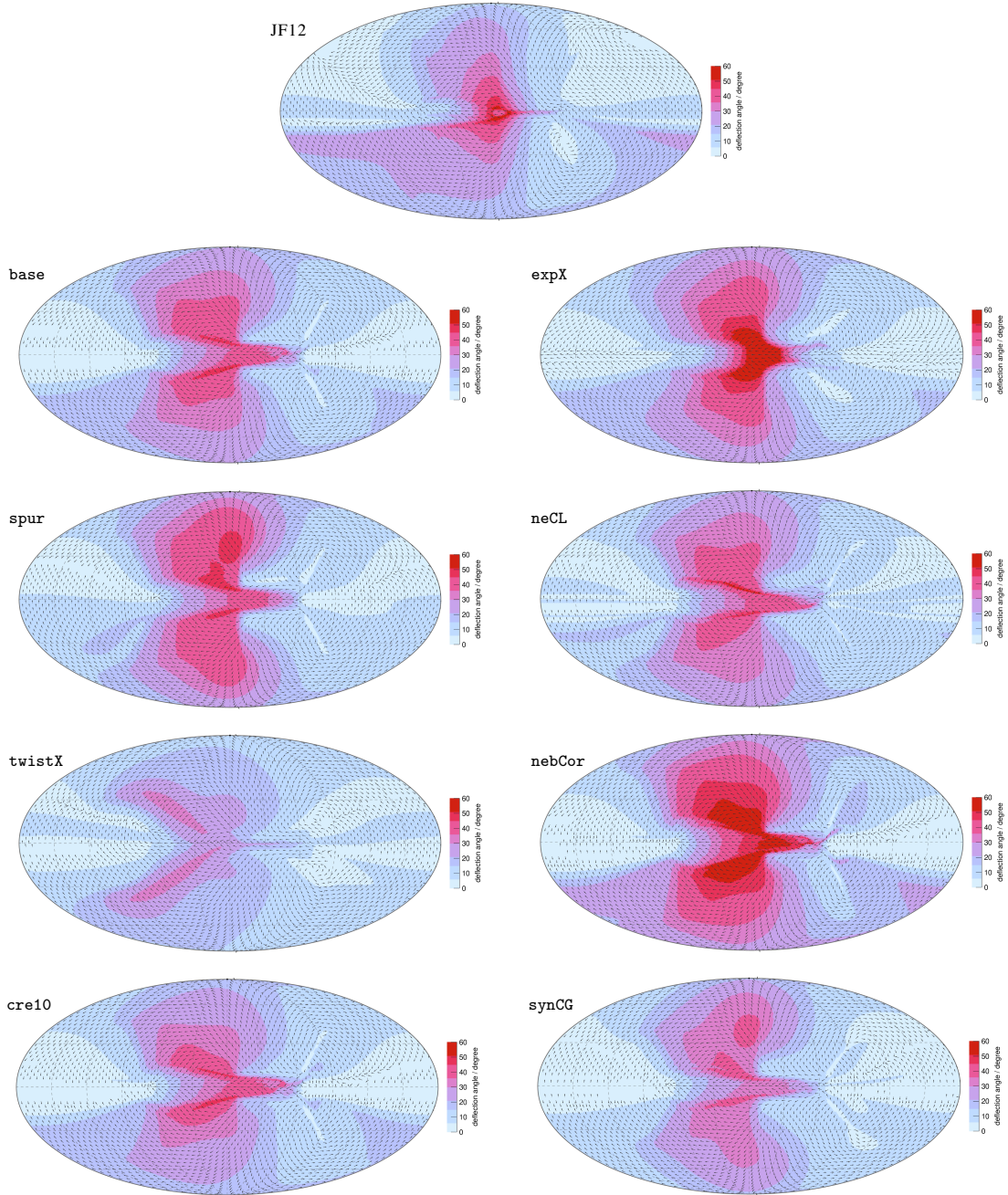


Figure 18. Angular deflections of ultrahigh-energy cosmic rays in JF12 model (top) and the eight model variations derived in this paper. Colors and arrows denote the size and direction of the deflection in the GMF following the particles from Earth to the edge of the Galaxy. Positions on the skymap denote arrival directions at Earth. The rigidity is 2×10^{19} V.

and u and v are connected by lines interpolating the backtracked directions at higher rigidities. This figure illustrates the similarity of the models, since in many directions all of them roughly agree on the overall direction of the deflection, but also shows the model uncertainties, visible as a scatter in predicted directions for the ensemble of models. It is worthwhile noting that the deflections predicted by the widely-used JF12 model are generally within the range of deflections pre-

dicted for the GMF models derived in this work. This is not the case for the deflections calculated with the GMF model of Pshirkov et al. (2011), due to the absence of a poloidal component in that model (c.f., Sec. 7.6).

Current studies of the anisotropies of ultrahigh-energy cosmic rays indicate the presence of “hot spots” of cosmic-ray clusters at intermediate angular scales of 20° (Abbasi et al. 2014; Abreu et al. 2022). For the identification of extragalac-

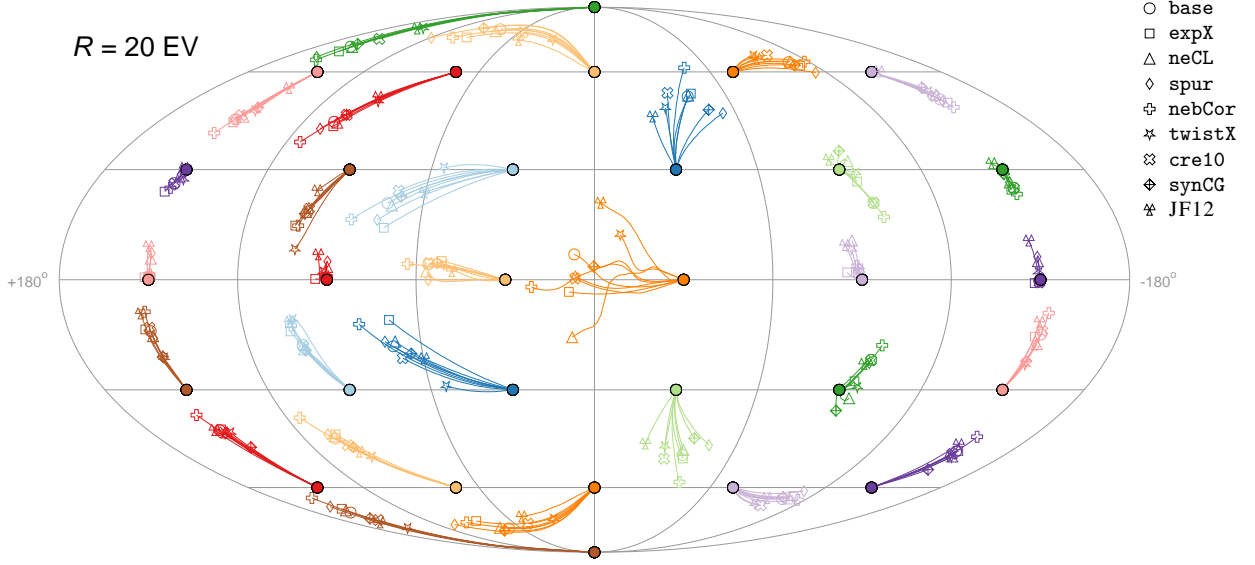


Figure 19. Angular deflections of ultrahigh-energy cosmic rays in the eight model variations derived in this paper and JF12. The cosmic-ray rigidity is 20 EV (2×10^{19} V). Filled circles denote a grid of arrival directions and the open symbols are the back-tracked directions at the edge of the Galaxy.

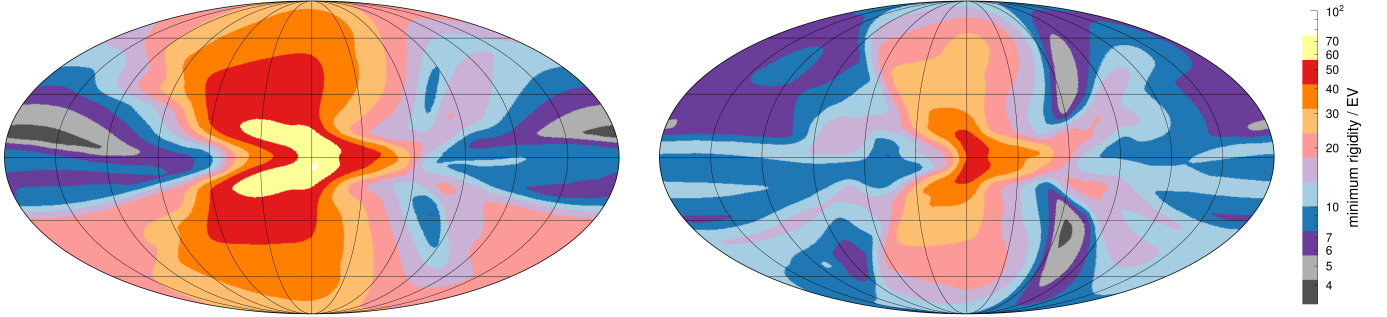


Figure 20. Left: Rigidity threshold such that the angular deflection in the given direction is $\leq 20^\circ$ in all models. Right: Rigidity threshold such that the model predictions of the angular deflection differ by $\leq 20^\circ$. (1 EV = 10^{18} V)

tic sources related to these overdensities, a precision in back-tracking through the GMF at least as good as their angular size, θ_{\max} , is needed. Figure 20 aims to illustrate this requirement. In the left panel, we show the minimum rigidity such that the deflection for a CR arriving in the given direction is less than $\theta_{\max} = 20^\circ$ in all 8 models. Requiring that the deflections in half of the sky are less than $\theta_{\max} = 20^\circ$, according to all of these models, requires the rigidity to be greater than or equal to $R_{50}^{\text{no corr}} = 20$ EV.

The minimum rigidity requirement improves considerably if the arrival directions are corrected for their expected deflection in the GMF. The limit on the precision with which we infer the source position arises from the *difference* between the models, and not the overall magnitude of the deflection. As can be seen from the right panel of Fig. 20, the required minimum rigidity is lower when the deflections are corrected for. This is because the differences of predicted deflections within the model ensemble are smaller than the deflections

themselves. With corrections, the rigidity quantile at which half of the sky can be observed at $\theta_{\max} = 20^\circ$ or better, decreases to $R_{50}^{\text{corr}} = 11$ EV giving a much greater observational reach. Note that this discussion is indicative only, since the minimal rigidity requirement may change when random fields are included in the analysis.

8.2. Axions

Another important application of the model ensemble presented in this paper is the prediction of the conversion of astrophysical axion-like particles (e.g. [Jaeckel & Ringwald 2010](#)) to photons in Galactic magnetic field. The general expression for axion-photon conversion in a plasma was derived by [Raffelt & Stodolsky \(1988\)](#). In the limit of small conversion probability, applicable due to known constraints, we can use the expression given in Eq. (S5) of ([Dessert et al. 2020](#)) for the axion-to-photon conversion probability between the source, located at r_{src} , and the observer located

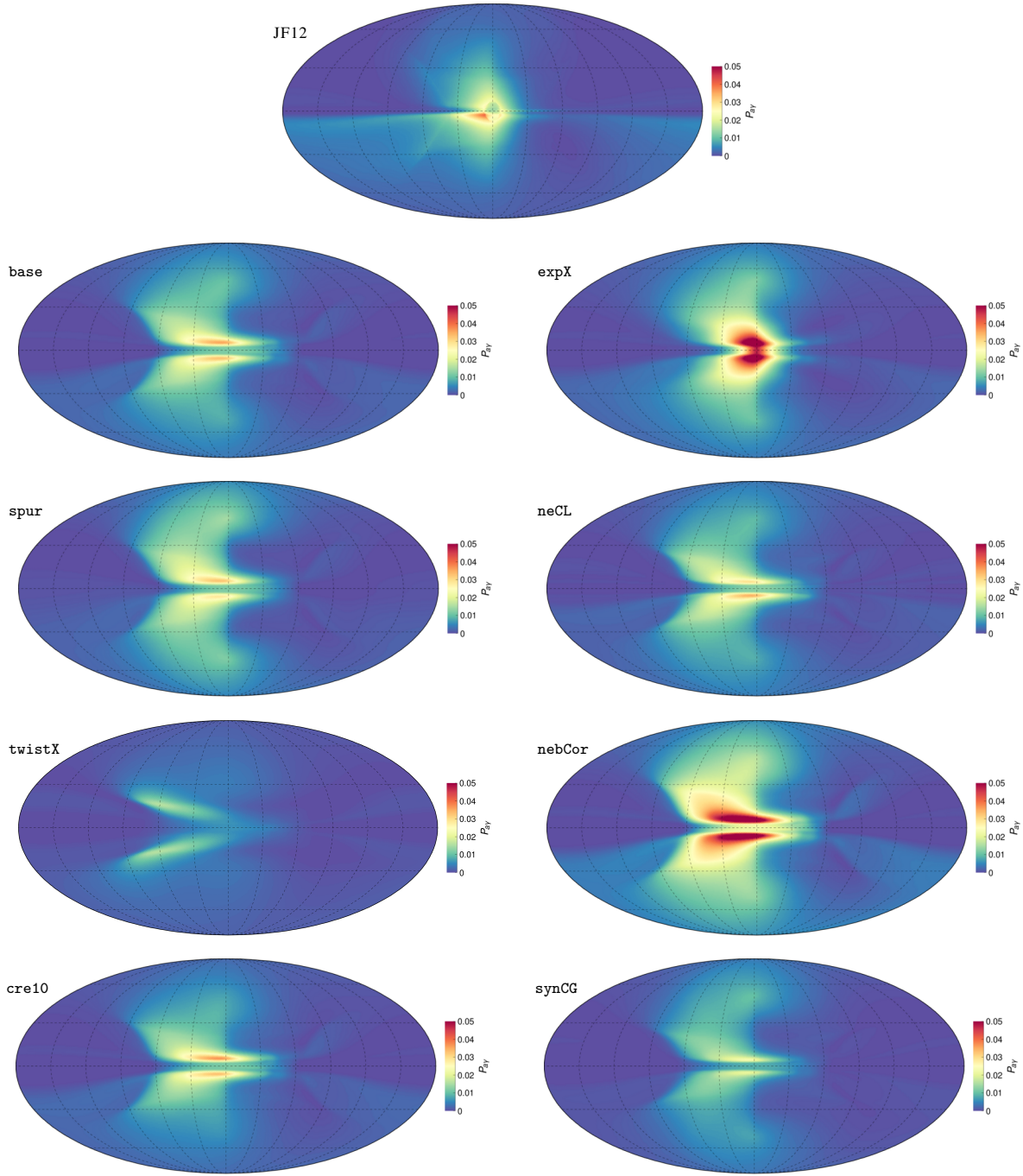


Figure 21. Axion-photon conversion probabilities, $p_{a\gamma}$, for the JF12 model (top), and the eight model variations derived in this paper ($g_{a\gamma\gamma} = 5 \times 10^{-12} \text{ GeV}^{-1}$, $E_a \gtrsim 1 \text{ TeV}$ and $m_a \lesssim 10^{-8} \text{ eV}$).

at the origin,

$$\begin{aligned}
 p_{a\gamma} &= \frac{g_{a\gamma\gamma}^2}{4} \sum_{i=1,2} \left| \int_{r_{\text{src}}}^0 dr B_i(r) e^{i\Delta_a r - i \int_{r_{\text{src}}}^r dr' \Delta_{\parallel}(r')} \right|^2 \\
 &\approx 2.3 \times 10^{-6} \left(\frac{g_{a\gamma\gamma}}{10^{-12} \text{ GeV}^{-1}} \sum_{i=1,2} \frac{\int_{r_{\text{src}}}^0 dr B_i(r)}{\text{kpc } \mu\text{G}} \right)^2. \quad (54)
 \end{aligned}$$

The integral is along the line of sight from source to observer and the subscripts $i = 1, 2$ refer to the transverse components of the magnetic field relative to the line of sight. Current limits on the axion-photon coupling strength are $g_{a\gamma\gamma} \lesssim \text{few} \times 10^{-12} \text{ GeV}^{-1}$ in the low axion-mass regime ($m_a \lesssim 10^{-6} \text{ eV}$) (Workman et al. 2022). The effective wave numbers entering the phase shift are $\Delta_a \equiv -m_a^2/(2E)$ and $\Delta_{\parallel}(r') \equiv -\omega_p(r')^2/(2E)$, where the plasma frequency

$\omega_p \approx 3.7 \times 10^{-12} (n_e / 10^{-2} \text{cm}^{-3})^{-1/2} \text{ eV}$. Thus, in the limit of large axion energies and low axion mass, the conversion probability simplifies to the last expression that depends only on the coupling constant and the line-of-sight integral of the traverse magnetic field as given in the second line of Eq. (54). We checked the validity range of this approximation by comparing it to the conversion probabilities in the JF12 magnetic field calculated with the gammaALPs package (Meyer et al. 2022) and found good agreement for $E_a \gtrsim 1 \text{ TeV}$ and $m_a \lesssim 10^{-8} \text{ eV}$.

The effect of the new magnetic field models derived in this paper on the predicted axion-photon conversion probabilities are shown in Fig. 21, where we assumed $g_{a\gamma\gamma} = 5 \times 10^{-12} \text{ GeV}^{-1}$. These figures look qualitatively very similar to the ones for the cosmic-ray deflections, Fig. 18, since both the conversion probability and the deflection depend on the perpendicular component of the magnetic field. The reason for the asymmetry of the conversion probability in longitude is again the twisted nature of the Galactic halo field. For a given extragalactic axion source candidate, the uncertainty of conversion probability can be estimated by finding the maximum and minimum prediction in the model ensemble in the direction of the source.

9. SUMMARY

In this paper we have developed new, improved models of the coherent magnetic field of the Milky Way, with better functional descriptions of the disk and poloidal fields of the Galaxy, as well as the first step toward a unified model for the toroidal and poloidal magnetic halo. We improve on previous analyses by using more and better variants of auxiliary models for the thermal and cosmic-ray electron densities. The parameters of these new models are constrained with the latest RM and PI data, which we have subjected to detailed scrutiny to resolve or reveal discrepancies.

Equipped with these improvements, and with a fast optimization framework that made it computationally feasible to investigate many model variations, we can infer the following insights about the coherent magnetic field of the Milky Way:

- The local pitch angle of the disk field is $(11 \pm 1)^\circ$.
- A magnetic field arranged as a grand-design spiral in the Galactic disk fits the data well; interestingly, the inferred field reversals occur at the position of tracers of the spiral arms of the matter density. However a grand-design spiral is not needed: a model with only a coherent local spur describes the RM and PI data equally well.
- Within the 10% statistical precision of the data, the magnitude of the toroidal halo field is the same below and above the disk.

- The vertical scale height of the inferred toroidal halo is anticorrelated to the assumed half-height of the cosmic-ray diffusion volume, with a lower 5- σ limit of $h_D \geq 2.9 \text{ kpc}$.
- Compatibility of the magnetic field strengths inferred from the RM and PI data can be achieved either through a striated random field having about the same energy density as the coherent field, or an anticorrelation between the thermal electrons and magnetic field strength with a coefficient of -0.4 .
- The new data corroborates the existence of the poloidal halo field introduced in JF12 with high significance. The strength of the poloidal field in the inner Galaxy is currently not well constrained due to the need for masking local structures.
- A simple unified halo model, in which the toroidal field is generated by the shearing of the poloidal field due to the Galactic rotation, fits the data well with only 6 instead of the usual 10 free halo parameters.

We selected an ensemble of eight model variations¹⁸ that encompass a large range of assumptions that are compatible with the data, see Table 2. As a first application, we employed these variations to study the deflections of ultrahigh-energy cosmic rays in the GMF. We find that the deflections predicted by the widely-used JF12 model are close to the ones from the new model ensemble. An important conclusion of our work is that the UHECR deflection uncertainties derived from the model ensemble are smaller than the deflection itself for most of the sky at ultrahigh energies, and we can localize the regions of greatest uncertainty.

The comprehensive study presented here significantly improves our knowledge of the global structure of the coherent magnetic field of the Milky Way, and for the first time provides a range of model possibilities to explore the impact of GMF uncertainties on GMF-sensitive science. However, it is just a step in the journey to achieving accurate knowledge of the magnetic field of the Galaxy. Directions for future improvements of the GMF modeling have been noted throughout this paper. These include a better understanding of Galactic foregrounds, an investigation of a possible position-dependence of the striation factor and a self-consistent modeling of the diffusion of cosmic-ray electrons in the GMF.

ACKNOWLEDGEMENTS

We would like to thank Rainer Beck, Katia Ferrière, Michael Kachelriess, Jens Kleimann and Darko Veberič for useful comments on this manuscript. MU acknowledges the support from the EU-funded Marie Curie Outgoing Fellowship, Grant PIOF-GA-2013-624803 for part of this work and the hospitality of CCPP/NYU. This research of GRF has

¹⁸A C++ implementation of these GMF models can be found at Unger & Farrar (2024).

been supported by NASA grant NNX10AC96G and NSF grants NSF-PHY-1212538, NSF-PHY-1517319, NSF-PHY-2013199, and by the Simons Foundation.

We acknowledge the use of the Legacy Archive for Microwave Background Data Analysis (LAMBDA), part of the High Energy Astrophysics Science Archive Center (HEASARC). HEASARC/LAMBDA is a service of the Astrophysics Science Division at the NASA Goddard Space

Flight Center. This work has benefited from discussions during the program "Towards a Comprehensive Model of the Galactic Magnetic Field" at NORDITA in April 2023, which is partly supported by NordForsk and Royal Astronomical Society.

Software: The results of this paper have been derived using the software packages HEALPIX (Górski et al. 2005), *Offline* (Argiro et al. 2007), and ROOT (Brun & Rademakers 1997).

REFERENCES

- Abbasi, R. U., et al. 2014, *Astrophys. J. Lett.*, 790, L21, doi: [10.1088/2041-8205/790/2/L21](https://doi.org/10.1088/2041-8205/790/2/L21)
- Abreu, P., et al. 2022, *Astrophys. J.*, 935, 170, doi: [10.3847/1538-4357/ac7d4e](https://doi.org/10.3847/1538-4357/ac7d4e)
- Abuter, R., Amorim, A., Bauböck, M., et al. 2019, *A&A*, 625, L10, doi: [10.1051/0004-6361/201935656](https://doi.org/10.1051/0004-6361/201935656)
- Ackermann, M., Albert, A., Atwood, W. B., et al. 2014, *ApJ*, 793, 64, doi: [10.1088/0004-637X/793/1/64](https://doi.org/10.1088/0004-637X/793/1/64)
- Adam, R., et al. 2016, *A&A*, 596, A103, doi: [10.1051/0004-6361/201528033](https://doi.org/10.1051/0004-6361/201528033)
- Ade, P. A. R., et al. 2014, *Astron. Astrophys.*, 566, A54, doi: [10.1051/0004-6361/201323003](https://doi.org/10.1051/0004-6361/201323003)
- Ade, P. A. R., Alves, M. I. R., Aniano, G., et al. 2015, *A&A*, 576, A107, doi: [10.1051/0004-6361/201424088](https://doi.org/10.1051/0004-6361/201424088)
- Adriani, O., et al. 2009, *Nature*, 458, 607, doi: [10.1038/nature07942](https://doi.org/10.1038/nature07942)
- Aguilar, M., et al. 2014, *Phys. Rev. Lett.*, 113, 221102, doi: [10.1103/PhysRevLett.113.221102](https://doi.org/10.1103/PhysRevLett.113.221102)
- . 2015, *Phys. Rev. Lett.*, 114, 171103, doi: [10.1103/PhysRevLett.114.171103](https://doi.org/10.1103/PhysRevLett.114.171103)
- . 2019, *Phys. Rev. Lett.*, 122, 041102, doi: [10.1103/PhysRevLett.122.041102](https://doi.org/10.1103/PhysRevLett.122.041102)
- Akrami, Y., Ashdown, M., Aumont, J., et al. 2020, *A&A*, 641, A4, doi: [10.1051/0004-6361/201833881](https://doi.org/10.1051/0004-6361/201833881)
- AL-Zetoun, A., & Achterberg, A. 2018, *MNRAS*, 477, 1258, doi: [10.1093/mnras/sty727](https://doi.org/10.1093/mnras/sty727)
- Anderson, C. S., Gaensler, B. M., Feain, I. J., & Franzen, T. M. O. 2015, *ApJ*, 815, 49, doi: [10.1088/0004-637X/815/1/49](https://doi.org/10.1088/0004-637X/815/1/49)
- Anderson, L. D., Bania, T. M., Balser, D. S., et al. 2014, *ApJS*, 212, 1, doi: [10.1088/0067-0049/212/1/1](https://doi.org/10.1088/0067-0049/212/1/1)
- Andreasyan, R. R., & Makarov, A. N. 1988, *Astrophysics*, 28, 247, doi: [10.1007/BF01004076](https://doi.org/10.1007/BF01004076)
- Argiro, S., Barroso, S., Gonzalez, J., et al. 2007, *Nucl. Instrum. Meth. A*, 580, 1485, doi: [10.1016/j.nima.2007.07.010](https://doi.org/10.1016/j.nima.2007.07.010)
- Beck, R. 2016, *A&A Rev.*, 24, 4, doi: [10.1007/s00159-015-0084-4](https://doi.org/10.1007/s00159-015-0084-4)
- Beck, R., Shukurov, A., Sokoloff, D., & Wielebinski, R. 2003, *A&A*, 411, 99, doi: [10.1051/0004-6361:20031101](https://doi.org/10.1051/0004-6361:20031101)
- Bennett, C. L., et al. 2013, *ApJS*, 208, 20, doi: [10.1088/0067-0049/208/2/20](https://doi.org/10.1088/0067-0049/208/2/20)
- Berkhuijsen, E. M., Haslam, C. G. T., & Salter, C. J. 1971, *A&A*, 14, 252
- Betti, S. K., Hill, A. S., Mao, S. A., et al. 2019, *ApJ*, 871, 215, doi: [10.3847/1538-4357/aaf886](https://doi.org/10.3847/1538-4357/aaf886)
- Blasi, P. 2023. <https://arxiv.org/abs/2307.11640>
- Bradt, H. 2008, *Astrophysics Processes* (Cambridge University Press), doi: [10.1080/00107510903471167](https://doi.org/10.1080/00107510903471167)
- Brandenburg, A., & Ntormousi, E. 2023, *ARA&A*, 61, 561, doi: [10.1146/annurev-astro-071221-052807](https://doi.org/10.1146/annurev-astro-071221-052807)
- Broderick, J. W., Bryant, J. J., Hunstead, R. W., Sadler, E. M., & Murphy, T. 2007, *MNRAS*, 381, 341, doi: [10.1111/j.1365-2966.2007.12277.x](https://doi.org/10.1111/j.1365-2966.2007.12277.x)
- Broten, N. W., MacLeod, J. M., & Vallee, J. P. 1988, *Ap&SS*, 141, 303, doi: [10.1007/BF00639497](https://doi.org/10.1007/BF00639497)
- Brown, J. C., Haverkorn, M., Gaensler, B. M., et al. 2007a, *ApJ*, 663, 258, doi: [10.1086/518499](https://doi.org/10.1086/518499)
- Brown, J. C., Taylor, A. R., & Jackel, B. J. 2003, *ApJS*, 145, 213, doi: [10.1086/346082](https://doi.org/10.1086/346082)
- Brown, J. C., et al. 2007b, *ApJ*, 663, 258, doi: [10.1086/518499](https://doi.org/10.1086/518499)
- Brun, R., & Rademakers, F. 1997, *Nucl. Instrum. Meth. A*, 389, 81, doi: [10.1016/S0168-9002\(97\)00048-X](https://doi.org/10.1016/S0168-9002(97)00048-X)
- Carretti, E., Crocker, R. M., Staveley-Smith, L., et al. 2013, *Nature*, 493, 66, doi: [10.1038/nature11734](https://doi.org/10.1038/nature11734)
- Cash, J., & Karp, A. 1990, *ACM Trans. Math. Soft.*, 16, 201, doi: [10.1145/79505.79507](https://doi.org/10.1145/79505.79507)
- Condon, J. J., Cotton, W. D., Greisen, E. W., et al. 1998, *AJ*, 115, 1693, doi: [10.1086/300337](https://doi.org/10.1086/300337)
- Cordes, J. M., & Lazio, T. J. W. 2002, *arXiv:0207156 [astro-ph]*
- Cummings, A. C., Stone, E. C., Heikkilä, B. C., et al. 2016, *ApJ*, 831, 18, doi: [10.3847/0004-637X/831/1/18](https://doi.org/10.3847/0004-637X/831/1/18)
- Dessert, C., Foster, J. W., & Safdi, B. R. 2020, *Phys. Rev. Lett.*, 125, 261102, doi: [10.1103/PhysRevLett.125.261102](https://doi.org/10.1103/PhysRevLett.125.261102)
- Di Bernardo, G., Evoli, C., Gaggero, D., Grasso, D., & Maccione, L. 2013, *JCAP*, 03, 036, doi: [10.1088/1475-7516/2013/03/036](https://doi.org/10.1088/1475-7516/2013/03/036)
- Di Mauro, M., Donato, F., Fornengo, N., Lineros, R., & Vittino, A. 2014, *JCAP*, 04, 006, doi: [10.1088/1475-7516/2014/04/006](https://doi.org/10.1088/1475-7516/2014/04/006)

- Evoli, C., Gaggero, D., Grasso, D., & Maccione, L. 2008, JCAP, 10, 018, doi: [10.1088/1475-7516/2008/10/018](https://doi.org/10.1088/1475-7516/2008/10/018)
- Evoli, C., Morlino, G., Blasi, P., & Aloisio, R. 2020, Phys. Rev. D, 101, 023013, doi: [10.1103/PhysRevD.101.023013](https://doi.org/10.1103/PhysRevD.101.023013)
- Farnes, J. S., Gaensler, B. M., & Carretti, E. 2014, ApJS, 212, 15, doi: [10.1088/0067-0049/212/1/15](https://doi.org/10.1088/0067-0049/212/1/15)
- Farrar, G. R. 2014, Comptes Rendus Physique, 15, 339, doi: [10.1016/j.crhy.2014.04.002](https://doi.org/10.1016/j.crhy.2014.04.002)
- Feain, I. J., Ekers, R. D., Murphy, T., et al. 2009, ApJ, 707, 114, doi: [10.1088/0004-637X/707/1/114](https://doi.org/10.1088/0004-637X/707/1/114)
- Ferrière, K., & Terral, P. 2014, A&A, 561, A100, doi: [10.1051/0004-6361/201322966](https://doi.org/10.1051/0004-6361/201322966)
- Ferrière, K., West, J. L., & Jaffe, T. R. 2021, MNRAS, 507, 4968, doi: [10.1093/mnras/stab1641](https://doi.org/10.1093/mnras/stab1641)
- Ferriere, K. M., Mac Low, M.-M., & Zweibel, E. G. 1991, ApJ, 375, 239, doi: [10.1086/170185](https://doi.org/10.1086/170185)
- Finkbeiner, D. P. 2003, ApJS, 146, 407, doi: [10.1086/374411](https://doi.org/10.1086/374411)
- Fletcher, R. 1970, The Computer Journal, 13, 317, doi: [10.1093/comjnl/13.3.317](https://doi.org/10.1093/comjnl/13.3.317)
- Fletcher, R., & Powell, M. J. D. 1963, The Computer Journal, 6, 163, doi: [10.1093/comjnl/6.2.163](https://doi.org/10.1093/comjnl/6.2.163)
- Gabici, S., Evoli, C., Gaggero, D., et al. 2019, Int. J. Mod. Phys. D, 28, 1930022, doi: [10.1142/S0218271819300222](https://doi.org/10.1142/S0218271819300222)
- Gaensler, B. M., Madsen, G. J., Chatterjee, S., & Mao, S. A. 2008, PASA, 25, 184, doi: [10.1071/AS08004](https://doi.org/10.1071/AS08004)
- Génolini, Y., et al. 2019, Phys. Rev. D, 99, 123028, doi: [10.1103/PhysRevD.99.123028](https://doi.org/10.1103/PhysRevD.99.123028)
- Giacinti, G., Kachelriess, M., & Semikoz, D. V. 2018, JCAP, 07, 051, doi: [10.1088/1475-7516/2018/07/051](https://doi.org/10.1088/1475-7516/2018/07/051)
- Ginzburg, V. L., & Syrovatskii, S. I. 1964, The Origin of Cosmic Rays (Pergamon Press)
- Goldreich, P., & Sridhar, S. 1995, ApJ, 438, 763, doi: [10.1086/175121](https://doi.org/10.1086/175121)
- Górski, K. M., Hivon, E., Banday, A. J., et al. 2005, ApJ, 622, 759, doi: [10.1086/427976](https://doi.org/10.1086/427976)
- Han, J. L., Manchester, R. N., Berkhuijsen, E. M., & Beck, R. 1997, A&A, 322, 98
- Han, J. L., Manchester, R. N., van Straten, W., & Demorest, P. 2018, ApJS, 234, 11, doi: [10.3847/1538-4365/aa9c45](https://doi.org/10.3847/1538-4365/aa9c45)
- Harvey-Smith, L., Madsen, G. J., & Gaensler, B. M. 2011, ApJ, 736, 83, doi: [10.1088/0004-637X/736/2/83](https://doi.org/10.1088/0004-637X/736/2/83)
- Haverkorn, M., & Heesen, V. 2012, Space Sci. Rev., 166, 133, doi: [10.1007/s11214-011-9757-0](https://doi.org/10.1007/s11214-011-9757-0)
- Heald, G., Braun, R., & Edmonds, R. 2009, A&A, 503, 409, doi: [10.1051/0004-6361/200912240](https://doi.org/10.1051/0004-6361/200912240)
- Heiles, C., Chu, Y. H., & Troland, T. H. 1981, ApJ, 247, L77, doi: [10.1086/183593](https://doi.org/10.1086/183593)
- Hogg, D. W., & Foreman-Mackey, D. 2018, Astrophys. J. Suppl., 236, 11, doi: [10.3847/1538-4365/aab76e](https://doi.org/10.3847/1538-4365/aab76e)
- Hooper, D., Blasi, P., & Serpico, P. D. 2009, JCAP, 01, 025, doi: [10.1088/1475-7516/2009/01/025](https://doi.org/10.1088/1475-7516/2009/01/025)
- Hou, L. G., & Han, J. L. 2014, A&A, 569, A125, doi: [10.1051/0004-6361/201424039](https://doi.org/10.1051/0004-6361/201424039)
- Iroshnikov, P. S. 1964, Soviet Ast., 7, 566
- Jaeckel, J., & Ringwald, A. 2010, Annual Review of Nuclear and Particle Science, 60, 405, doi: [10.1146/annurev.nucl.012809.104433](https://doi.org/10.1146/annurev.nucl.012809.104433)
- Jaffe, T. R. 2017, private communication
- . 2019, Galaxies, 7, 52, doi: [10.3390/galaxies7020052](https://doi.org/10.3390/galaxies7020052)
- Jaffe, T. R., Leahy, J. P., Banday, A. J., et al. 2010, MNRAS, 401, 1013, doi: [10.1111/j.1365-2966.2009.15745.x](https://doi.org/10.1111/j.1365-2966.2009.15745.x)
- James, F., & Roos, M. 1975, Comp. Phys. Comm., 10, 343, doi: [10.1016/0010-4655\(75\)90039-9](https://doi.org/10.1016/0010-4655(75)90039-9)
- Jansson, R., & Farrar, G. R. 2012a, ApJ, 757, 14, doi: [10.1088/0004-637X/757/1/14](https://doi.org/10.1088/0004-637X/757/1/14)
- . 2012b, ApJ, 761, L11, doi: [10.1088/2041-8205/761/1/L11](https://doi.org/10.1088/2041-8205/761/1/L11)
- Jansson, R., Farrar, G. R., Waelkens, A. H., & Ensslin, T. A. 2009, JCAP, 07, 021, doi: [10.1088/1475-7516/2009/07/021](https://doi.org/10.1088/1475-7516/2009/07/021)
- Joshi, J. C., & Razzaque, S. 2017, JCAP, 09, 029, doi: [10.1088/1475-7516/2017/09/029](https://doi.org/10.1088/1475-7516/2017/09/029)
- Joshi, Y. C., Dambis, A. K., Pandey, A. K., & Joshi, S. 2016, A&A, 593, A116, doi: [10.1051/0004-6361/201628944](https://doi.org/10.1051/0004-6361/201628944)
- Kaczmarek, J. F., Purcell, C. R., Gaensler, B. M., McClure-Griffiths, N. M., & Stevens, J. 2017, MNRAS, 467, 1776, doi: [10.1093/mnras/stx206](https://doi.org/10.1093/mnras/stx206)
- Kalberla, P. M. W., & Kerp, J. 2009, ARA&A, 47, 27, doi: [10.1146/annurev-astro-082708-101823](https://doi.org/10.1146/annurev-astro-082708-101823)
- Khurana, D. 2016, (private communication)
- Kleimann, J., Schorlepp, T., Merten, L., & Becker Tjus, J. 2019, ApJ, 877, 76, doi: [10.3847/1538-4357/ab1913](https://doi.org/10.3847/1538-4357/ab1913)
- Klein, U., Mack, K.-H., Gregorini, L., & Vigotti, M. 2003, A&A, 406, 579, doi: [10.1051/0004-6361:20030825](https://doi.org/10.1051/0004-6361:20030825)
- Kraichnan, R. H. 1965, The Physics of Fluids, 8, 1385, doi: [10.1063/1.1761412](https://doi.org/10.1063/1.1761412)
- Krause, M., Irwin, J., Schmidt, P., et al. 2020, A&A, 639, A112, doi: [10.1051/0004-6361/202037780](https://doi.org/10.1051/0004-6361/202037780)
- Kuhlen, M., Phan, V. H. M., & Mertsch, P. 2022, <https://arxiv.org/abs/2211.05882>
- Laing, R. A. 1980, MNRAS, 193, 439, doi: [10.1093/mnras/193.3.439](https://doi.org/10.1093/mnras/193.3.439)
- Lallement, R. 2022, arXiv e-prints, arXiv:2203.01312, doi: [10.48550/arXiv.2203.01312](https://doi.org/10.48550/arXiv.2203.01312)
- Levine, E. S., Blitz, L., & Heiles, C. 2006, ApJ, 643, 881, doi: [10.1086/503091](https://doi.org/10.1086/503091)
- Levine, E. S., Heiles, C., & Blitz, L. 2008, ApJ, 679, 1288, doi: [10.1086/587444](https://doi.org/10.1086/587444)
- Longair, M. S. 2011, High Energy Astrophysics (Cambridge University Press)

- Lorimer, D. R., Faulkner, A. J., Lyne, A. G., et al. 2006, *MNRAS*, 372, 777, doi: [10.1111/j.1365-2966.2006.10887.x](https://doi.org/10.1111/j.1365-2966.2006.10887.x)
- Ma, Y. K., Mao, S. A., Ordog, A., & Brown, J. C. 2020, *MNRAS*, 497, 3097, doi: [10.1093/mnras/staa2105](https://doi.org/10.1093/mnras/staa2105)
- Ma, Y. K., Mao, S. A., Stil, J., et al. 2019, *MNRAS*, 487, 3432, doi: [10.1093/mnras/stz1325](https://doi.org/10.1093/mnras/stz1325)
- Majaess, D. J., Turner, D. G., & Lane, D. J. 2009, *MNRAS*, 398, 263, doi: [10.1111/j.1365-2966.2009.15096.x](https://doi.org/10.1111/j.1365-2966.2009.15096.x)
- Manchester, R. N. 1972, *ApJ*, 172, 43, doi: [10.1086/151326](https://doi.org/10.1086/151326)
- Manchester, R. N., Hobbs, G. B., Teoh, A., & Hobbs, M. 2005, *AJ*, 129, 1993, doi: [10.1086/428488](https://doi.org/10.1086/428488)
- Mao, S. A., Gaensler, B. M., Haverkorn, M., et al. 2010, *ApJ*, 714, 1170, doi: [10.1088/0004-637X/714/2/1170](https://doi.org/10.1088/0004-637X/714/2/1170)
- Mao, S. A., McClure-Griffiths, N. M., Gaensler, B. M., et al. 2012a, *ApJ*, 755, 21, doi: [10.1088/0004-637X/755/1/21](https://doi.org/10.1088/0004-637X/755/1/21)
- . 2012b, *ApJ*, 759, 25, doi: [10.1088/0004-637X/759/1/25](https://doi.org/10.1088/0004-637X/759/1/25)
- Maurin, D., Donato, F., Taillet, R., & Salati, P. 2001, *ApJ*, 555, 585, doi: [10.1086/321496](https://doi.org/10.1086/321496)
- Maurin, D., Ferronato Bueno, E., & Derome, L. 2022, *Astron. Astrophys.*, 667, A25, doi: [10.1051/0004-6361/202243546](https://doi.org/10.1051/0004-6361/202243546)
- Men, H., & Han, J. L. 2003, *Acta Astronomica Sinica*, 44, 151
- Merten, L., Becker Tjus, J., Fichtner, H., Eichmann, B., & Sigl, G. 2017, *JCAP*, 06, 046, doi: [10.1088/1475-7516/2017/06/046](https://doi.org/10.1088/1475-7516/2017/06/046)
- Mertsch, P. 2018, *JCAP*, 11, 045, doi: [10.1088/1475-7516/2018/11/045](https://doi.org/10.1088/1475-7516/2018/11/045)
- Meyer, M., Davies, J., & Kuhlmann, J. 2022, in 37th International Cosmic Ray Conference, 557, doi: [10.22323/1.395.0557](https://doi.org/10.22323/1.395.0557)
- Moskalenko, I. V., & Strong, A. W. 1998, *ApJ*, 493, 694, doi: [10.1086/305152](https://doi.org/10.1086/305152)
- Orlando, E. 2018, *MNRAS*, 475, 2724, doi: [10.1093/mnras/stx3280](https://doi.org/10.1093/mnras/stx3280)
- Orlando, E., & Strong, A. 2013, *MNRAS*, 436, 2127, doi: [10.1093/mnras/stt1718](https://doi.org/10.1093/mnras/stt1718)
- O’Sullivan, S. P., Purcell, C. R., Anderson, C. S., et al. 2017, *MNRAS*, 469, 4034, doi: [10.1093/mnras/stx1133](https://doi.org/10.1093/mnras/stx1133)
- O’Sullivan, S. P., Shimwell, T. W., Hardcastle, M. J., et al. 2023, *MNRAS*, 519, 5723, doi: [10.1093/mnras/stac3820](https://doi.org/10.1093/mnras/stac3820)
- Pakmor, R., Guillet, T., Pfrommer, C., et al. 2018, *MNRAS*, 481, 4410, doi: [10.1093/mnras/sty2601](https://doi.org/10.1093/mnras/sty2601)
- Pakmor, R., Marinacci, F., & Springel, V. 2014, *Astrophys. J. Lett.*, 783, L20, doi: [10.1088/2041-8205/783/1/L20](https://doi.org/10.1088/2041-8205/783/1/L20)
- Parker, E. N. 1979, *Cosmical magnetic fields: Their origin and their activity* (Oxford University Press)
- Porter, T. A., Jóhannesson, G., & Moskalenko, I. V. 2017, *ApJ*, 846, 67, doi: [10.3847/1538-4357/aa844d](https://doi.org/10.3847/1538-4357/aa844d)
- Predehl, P., Sunyaev, R. A., Becker, W., et al. 2020, *Nature*, 588, 227, doi: [10.1038/s41586-020-2979-0](https://doi.org/10.1038/s41586-020-2979-0)
- Price, D. C., Flynn, C., & Deller, A. 2021, *PASA*, 38, e038, doi: [10.1017/pasa.2021.33](https://doi.org/10.1017/pasa.2021.33)
- Prouza, M., & Šmída, R. 2003, *A&A*, 410, 1, doi: [10.1051/0004-6361:20031281](https://doi.org/10.1051/0004-6361:20031281)
- Pshirkov, M. S., Tinyakov, P. G., Kronberg, P. P., & Newton-McGee, K. J. 2011, *ApJ*, 738, 192, doi: [10.1088/0004-637X/738/2/192](https://doi.org/10.1088/0004-637X/738/2/192)
- Raffelt, G., & Stodolsky, L. 1988, *Phys. Rev. D*, 37, 1237, doi: [10.1103/PhysRevD.37.1237](https://doi.org/10.1103/PhysRevD.37.1237)
- Reid, M. J., et al. 2014, *ApJ*, 783, 130, doi: [10.1088/0004-637X/783/2/130](https://doi.org/10.1088/0004-637X/783/2/130)
- Reid, M. J., Menten, K. M., Brunthaler, A., et al. 2019, *ApJ*, 885, 131, doi: [10.3847/1538-4357/ab4a11](https://doi.org/10.3847/1538-4357/ab4a11)
- Riseley, C. J., Galvin, T. J., Sobey, C., et al. 2020, *PASA*, 37, e029, doi: [10.1017/pasa.2020.20](https://doi.org/10.1017/pasa.2020.20)
- Ryden, B., & Pogge, R. W. 2021, *Interstellar and Intergalactic Medium* (Cambridge University Press), doi: [10.1017/9781108781596](https://doi.org/10.1017/9781108781596)
- Schnitzeler, D. H. F. M. 2012, *MNRAS*, 427, 664, doi: [10.1111/j.1365-2966.2012.21869.x](https://doi.org/10.1111/j.1365-2966.2012.21869.x)
- Schnitzeler, D. H. F. M., Carretti, E., Wieringa, M. H., et al. 2019, *MNRAS*, 485, 1293, doi: [10.1093/mnras/stz092](https://doi.org/10.1093/mnras/stz092)
- Schwarz, G. 1978, *Annals of Statistics*, 6, 461
- Seta, A., & Federrath, C. 2021, *Physical Review Fluids*, 6, 103701, doi: [10.1103/PhysRevFluids.6.103701](https://doi.org/10.1103/PhysRevFluids.6.103701)
- Simard-Normandin, M., Kronberg, P. P., & Button, S. 1981, *ApJS*, 45, 97, doi: [10.1086/190709](https://doi.org/10.1086/190709)
- Spoelstra, T. A. T. 1973, *A&A*, 24, 149
- Stanev, T. 1997, *ApJ*, 479, 290, doi: [10.1086/303866](https://doi.org/10.1086/303866)
- Strong, A. W., & Moskalenko, I. V. 1998, *ApJ*, 509, 212, doi: [10.1086/306470](https://doi.org/10.1086/306470)
- Sun, X.-H., & Reich, W. 2010, *Research in Astronomy and Astrophysics*, 10, 1287, doi: [10.1088/1674-4527/10/12/009](https://doi.org/10.1088/1674-4527/10/12/009)
- Sun, X. H., Reich, W., Waelkens, A., & Enßlin, T. A. 2008, *A&A*, 477, 573, doi: [10.1051/0004-6361:20078671](https://doi.org/10.1051/0004-6361:20078671)
- Svalheim, T. L., et al. 2023, *Astron. Astrophys.*, 675, A9, doi: [10.1051/0004-6361/202243080](https://doi.org/10.1051/0004-6361/202243080)
- Taylor, A. R., Stil, J. M., & Sunstrum, C. 2009, *ApJ*, 702, 1230, doi: [10.1088/0004-637X/702/2/1230](https://doi.org/10.1088/0004-637X/702/2/1230)
- Terral, P., & Ferrière, K. 2017, *A&A*, 600, A29, doi: [10.1051/0004-6361/201629572](https://doi.org/10.1051/0004-6361/201629572)
- Unger, M., & Farrar, G. R. 2018, *PoS(ICRC2017)*, 558, doi: [10.22323/1.301.0558](https://doi.org/10.22323/1.301.0558)
- . 2019, *EPJ Web Conf.*, 210, 04005, doi: [10.1051/epjconf/201921004005](https://doi.org/10.1051/epjconf/201921004005)
- . 2024, *The Coherent Magnetic Field of the Milky Way*, v1.0, Zenodo, doi: [10.5281/zenodo.10627090](https://doi.org/10.5281/zenodo.10627090)
- Vallée, J. P. 2022, *New A*, 97, 101896, doi: [10.1016/j.newast.2022.101896](https://doi.org/10.1016/j.newast.2022.101896)
- Van Eck, C. L., Brown, J. C., Shukurov, A., & Fletcher, A. 2015, *ApJ*, 799, 35, doi: [10.1088/0004-637X/799/1/35](https://doi.org/10.1088/0004-637X/799/1/35)

- Van Eck, C. L., Brown, J. C., Stil, J. M., et al. 2011, *ApJ*, 728, 97, doi: [10.1088/0004-637X/728/2/97](https://doi.org/10.1088/0004-637X/728/2/97)
- Van Eck, C. L., Brown, J. C., Ordog, A., et al. 2021, *ApJS*, 253, 48, doi: [10.3847/1538-4365/abe389](https://doi.org/10.3847/1538-4365/abe389)
- Van Eck, C. L., Gaensler, B. M., Hutschenreuter, S., et al. 2022, RMTable Consolidated Catalog of Faraday Rotation Measures of Astronomical Radio Sources, v1.1.0, Zenodo, doi: [10.5281/zenodo.7894467](https://doi.org/10.5281/zenodo.7894467)
- Van Eck, C. L., Gaensler, B. M., Hutschenreuter, S., et al. 2023, *ApJS*, 267, 28, doi: [10.3847/1538-4365/acda24](https://doi.org/10.3847/1538-4365/acda24)
- Vidal, M., Dickinson, C., Davies, R. D., & Leahy, J. P. 2015, *MNRAS*, 452, 656, doi: [10.1093/mnras/stv1328](https://doi.org/10.1093/mnras/stv1328)
- Wardle, J. F. C., & Kronberg, P. P. 1974, *ApJ*, 194, 249, doi: [10.1086/153240](https://doi.org/10.1086/153240)
- Watts, D. J., Basyrov, A., Eskilt, J. R., et al. 2023a, arXiv e-prints, arXiv:2303.08095, doi: [10.48550/arXiv.2303.08095](https://doi.org/10.48550/arXiv.2303.08095)
- Watts, D. J., Fuskeland, U., Aurlen, R., et al. 2023b, arXiv e-prints, arXiv:2310.13740, doi: [10.48550/arXiv.2310.13740](https://doi.org/10.48550/arXiv.2310.13740)
- Weinrich, N., Boudaud, M., Derome, L., et al. 2020, *Astron. Astrophys.*, 639, A74, doi: [10.1051/0004-6361/202038064](https://doi.org/10.1051/0004-6361/202038064)
- Wilks, S. S. 1938, *Annals Math. Statist.*, 9, 60, doi: [10.1214/aoms/1177732360](https://doi.org/10.1214/aoms/1177732360)
- Workman, R. L., et al. 2022, *PTEP*, 2022, 083C01, doi: [10.1093/ptep/ptac097](https://doi.org/10.1093/ptep/ptac097)
- Xu, J., & Han, J.-L. 2014, *RAA*, 14, 942, doi: [10.1088/1674-4527/14/8/005](https://doi.org/10.1088/1674-4527/14/8/005)
- Yao, J. M., Manchester, R. N., & Wang, N. 2017, *ApJ*, 835, 29, doi: [10.3847/1538-4357/835/1/29](https://doi.org/10.3847/1538-4357/835/1/29)
- Yuan, Q., Lin, S.-J., Fang, K., & Bi, X.-J. 2017, *Phys. Rev. D*, 95, 083007, doi: [10.1103/PhysRevD.95.083007](https://doi.org/10.1103/PhysRevD.95.083007)

APPENDIX: COMPARISON OF SYNCHROTRON DATA PRODUCTS

Sky maps of the Stokes Q and U parameters of the polarized synchrotron emission are shown in the sub-panels along the diagonal of Figs. 22. The values are from the 9-year WMAP “base” model (Bennett et al. 2013), the third PLANCK data release (DR3.0) (Akrami et al. 2020), our simple arithmetic average of WMAP and PLANCK, and the CosmoGlobe results derived from a combined analysis of WMAP and PLANCK data (Watts et al. 2023a). The difference between each data set is shown as sky maps in the off-diagonal panels. As can be seen, the WMAP and PLANCK maps exhibit large differences in the Galactic plane, that could be related to different levels of temperature-to-polarization leakage in the two data sets (Svalheim et al. 2023). This region of the sky is, however, not relevant for our analysis as it is masked in fit. Moreover, there are large-scale systematic differences between the Q and U parameters derived by the two collaborations. Our arithmetic average is by construction in between the two data products and the values from the global reanalysis from CosmoGlobe show yet another large-scale distribution of Q and U differences.

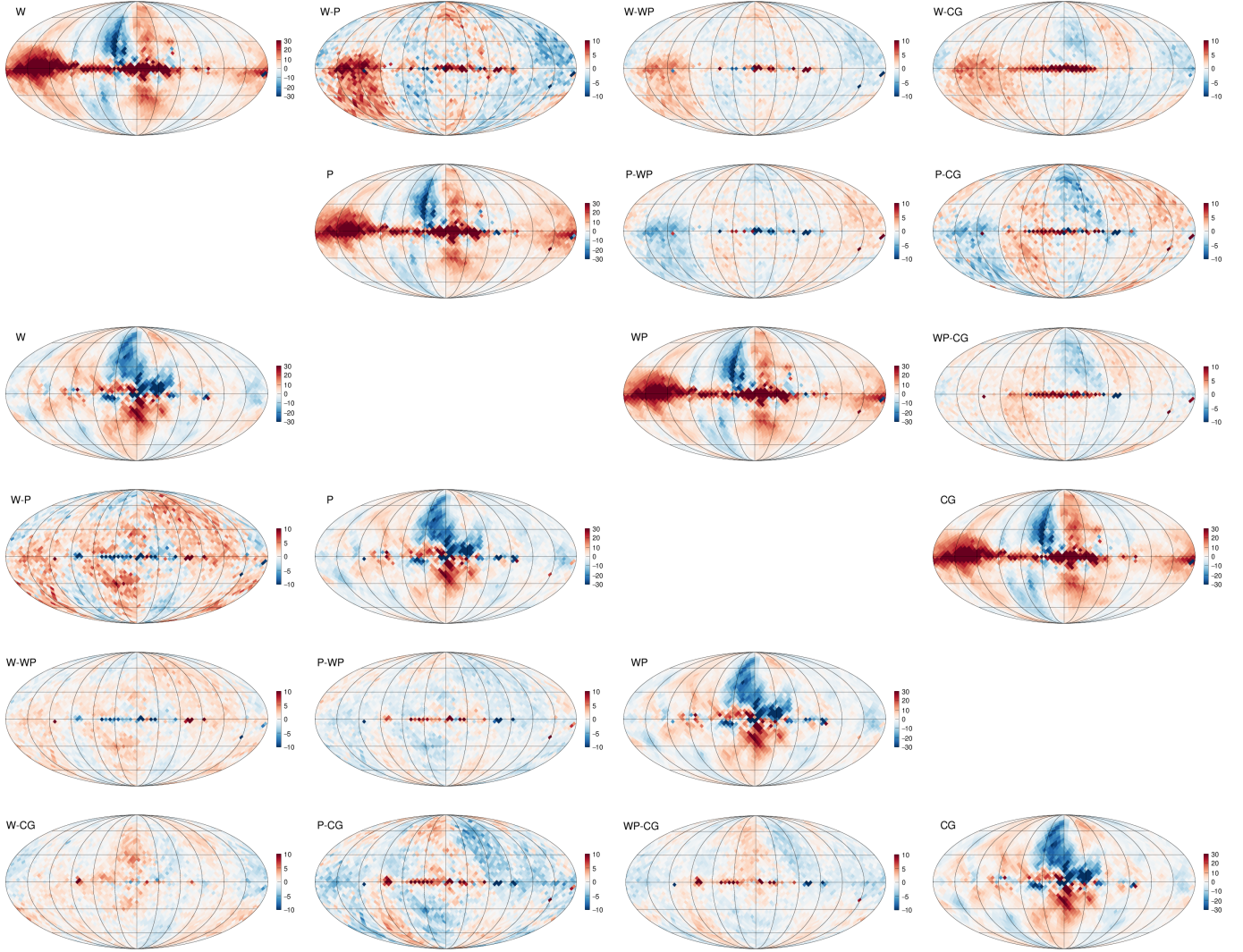


Figure 22. Values (diagonal) and differences (off-diagonal) of Stokes parameters at 30 GHz in μK of WMAP (W), PLANCK (P), our arithmetic average of WMAP and PLANCK (WP), and the WMAP-PLANCK combination of the CosmoGlobe collaboration (CG). Stokes Q parameters are shown as an upper triangular matrix of plots at the top, Stokes U parameters are displayed as a lower triangular matrix of plots at the bottom. Values are given in μK .